remote sensing

MDPI

Article

Assessment of the Accuracy of Terrestrial Laser Scanners in Detecting Local Surface Anomaly

Ali Algadhi [1,2,3], Panos Psimoulis [2,3,*], Athina Grizi [4] and Luis Neves [3]

[1] Department of Civil Engineering, King Saud University, Riyadh 11421, Saudi Arabia; aalgadhi@ksu.edu.sa
[2] Nottingham Geospatial Institute, University of Nottingham, Nottingham NG7 2TU, UK
[3] Department of Civil Engineering, University of Nottingham, Nottingham NG7 2RD, UK; luis.neves@nottingham.ac.uk
[4] Region of Western Greece, 26443 Patras, Greece; a.grizi@pde.gov.gr
* Correspondence: panagiotis.psimoulis@nottingham.ac.uk

Abstract: The surface anomaly is a common defect for structures that resist lateral stresses, such as retaining walls. The accurate detection of an anomaly using contactless techniques, such as the Terrestrial Laser Scanner (TLS), is significant for the reliable structural assessment. The influence of the scanning geometry on the accuracy of the TLS point-clouds was investigated in previous studies; however, a deeper analysis is needed to investigate their impact in the context of structural health monitoring. This paper aims to empirically assess the performance of the TLS in detecting surface anomalies, with respect to the scanning distance and angle of incidence in two cases: (i) when both the reference and deformed clouds are taken from the same scanning position, and (ii) the scans are from different positions. Furthermore, the paper examines the accuracy of estimating the depth of the anomaly using three cloud comparison techniques (i.e., C2C, C2M, and M3C2 methods). The results show that the TLS is capable of detecting the surface anomaly for distances between 2 and 30 m and angles of incidence between 90° and 30°, with a tolerance of within a few millimeters. This is achieved even for the case where scans from different locations (i.e., angles and distances) are applied.

Keywords: TLS; SHM; surface anomaly; change detection; C2C; C2M; M3C2; LiDAR

check for updates

Citation: Algadhi, A.; Psimoulis, P.; Grizi, A.; Neves, L. Assessment of the Accuracy of Terrestrial Laser Scanners in Detecting Local Surface Anomaly. *Remote Sens.* **2024**, *16*, 4647. https://doi.org/10.3390/rs16244647

Academic Editor: Giuseppe Casula

Received: 3 November 2024
Revised: 3 December 2024
Accepted: 9 December 2024
Published: 11 December 2024

Copyright: © 2024 by the authors. Licensee MDPI, Basel, Switzerland. This article is an open access article distributed under the terms and conditions of the Creative Commons Attribution (CC BY) license (https://creativecommons.org/licenses/by/4.0/).

1. Introduction

Many types of infrastructures are designed to resist lateral stresses from water/soil, such as retaining walls and dams [1]. The lateral pressure can result in a lateral displacement, either throughout the wall height or at a limited area, i.e., surface anomaly/bulge [2]. These deformations are significant, as they are used as serviceability measures to assess the health state of the structures. The surface anomaly has been reported extensively; for example, about 60% of the reported cases of geosynthetic reinforced walls with serviceability problems in Koerner and Soong [3] had bulges at various locations of the walls. The structural assessment of these structures should be conducted by a technique with high accuracy. For instance, Highways England Standards [4] recommend a tolerance of 10 mm for the structural assessment of retaining structures.

Various techniques have been used for detecting the relative lateral displacements; some are contact based, e.g., inclinometer, and some are contactless, e.g., LiDAR sensors [5]. The LiDAR sensor can also be used for the change detection of the surfaces, such as the case of Lerones et al. [6] and Suchocki and Katzer [7] for detecting moisture in structures; Chen et al. [8] for the material loss, concrete erosion and reinforcement corrosion; and Turkan et al. [9] and Chen et al. [10] for detecting cracks in concrete surfaces. However, the identification of local anomalies (e.g., bulge) is yet to be assessed under controlled experiment.

Furthermore, the accuracy of the contactless techniques, specifically the Terrestrial Laser Scanner (TLS), has been of great research interest in recent years due to its practical and accurate measurements [11]. Bolkas and Martinez [12] studied the impact of the color of the scanned surface as well as the scanning distance and angle of incidence on the accuracy of the TLS by studying the residuals of the fitted planes for the scanned surfaces. The plane residuals were varied between 1 and 4 mm depending on the material, color, distance, and incidence angle. Bauer and Woschitz [13] studied the accuracy of the TLS in measuring the distance of various types of targets, and they found agreement between the TLS and the total station of about 1–2 mm. However, these studies focused on the accuracy of the TLS measurements for each scan independently, while a deeper analysis is necessary to assess the accuracy of the deformation estimation between two scans [11,14], as, for instance, the error in the angle of incidence may be mitigated if both scans that are taken prior to and after the deformation are acquired from the same scanning position.

The accuracy of the deformation estimation depends also on the method of comparing the two clouds [15]. In general, these methods can be classified into two main approaches: (i) the Piecewise Alignment Method (PAM), which estimates the transformation parameters (i.e., translations and rotations) that align a selected piece in the deformed point-cloud (e.g., point, line or shape) with the corresponding piece in the reference cloud using the Iterative Closest Point (ICP) technique, and (ii) distance measurements between the two clouds using the points and meshes, e.g., estimating the distance between each point in the deformed cloud and its closest point in the reference cloud [16,17]. The main difference between the two methods is that the former assumes that the two pieces in the reference and deformed clouds are practically the same, and attempts to find the best fit for them. Consequently, the first method is more applicable for the registration of two point-clouds, whereas the latter is more applicable for deformation analysis applications [17].

From the distance measurement approach, three main techniques have been widely used for monitoring the geometric deformations in point-clouds; the Cloud to Cloud (C2C), Cloud to Mesh (C2M), and Multiscale Model-to-Model Cloud Comparison (M3C2). The C2C method is introduced by calculating the distance from each point in the deformed scan (i.e., the latter epoch) to its nearest point in the reference scan (i.e., the first epoch) [18]. The same methodology is applied by the C2M method with one change: creating a surface mesh for the reference cloud, and then calculating the shortest distance from each point in the deformed cloud to the surface mesh of the reference cloud [19]. The distance using the M3C2 method is calculated by first estimating the direction of the distance measurement, and then calculating the distance between local surfaces in the reference and deformed scans [17]. The C2C method is the simplest and fastest, but it is influenced, as well as the M3C2, by the roughness of the point-clouds and the outliers [19]. The M3C2 method is considered more accurate, but it requires a long calculation time [17]. The C2M method does not require input parameters, such those for the M3C2 method, but provides only the Euclidean distance (i.e., not at the desired direction) [20].

The C2C, C2M, and M3C2 methods have been used in many research papers for estimating geometric deformations, such as Acikgoz et al. [16] for monitoring the settlement of a vaulted masonry structure; Seo et al. [18] for monitoring the lateral displacement of a retaining wall; Kim et al. [21] for detecting the manual introduced deformation in a retaining wall under a controlled environment; and Makuch et al. [22] to estimate the thickness of hyperboloid cooling towers by scanning the internal and external surfaces of the structure. Algadhi et al. [23] also investigated the performance of these methods for detecting absolute lateral displacement (i.e., throughout the wall height) under controlled experiments. However, the accuracy of these methods in detecting and calculating the magnitude of local anomalies (e.g., bulge on the wall) is yet to be investigated under controlled experiment.

Several factors can influence the accuracy of the anomaly detection using the TLS point-clouds, but the main influence factors are the scanning range, the angle of incidence, and the method of cloud comparison between the two clouds, prior to and after the

deformation. Although these factors might have already been studied in terms of their influence on the accuracy of each point-cloud individually, their impact in the context of comparing two clouds has not been explicitly assessed. The scope of this study is to investigate the performance of the TLS in monitoring the local deformation of a civil engineering structure, developed as a local anomaly of the surface or as part of a broader deformation of the structure, which is a common type of deformation for retaining walls and brick walls. The paper contributes to two areas: (i) identification of the local anomaly within the monitored surface, and (ii) evaluation of the accuracy of the C2C, C2M, and M3C2 methods for the estimation of the depth of the local anomaly. First, we examine various techniques for the change detection to identify the local anomaly, including (i) the change in intensity of the reflected laser, (ii) the change in the direction of the normal vector, and (iii) the change in the position of the reflected points. Then, we investigate the impact of the scanning distance, scanning angle, and method of calculating the displacement on the accuracy of the depth of the local anomaly.

This study is based on a controlled experiment where the performance of the TLS is assessed by examining the impact of (i) the parameters of the scanning distance and scanning angle when the scans are taken from the same scanning position, and (ii) the impact of changing the scanning position, between the reference point-cloud and the point-clouds of the various deformed states. The novelty of this study lies in the holistic and multi-parametric approach to the identification of potential local deformation on the surface of civil engineering structures as well as the accurate estimation of the depth of the local anomaly. Finally, the approach of this study is applied on the surface of a real civil engineering structure to validate the developed approach of the experiment in real conditions.

2. Experiment

The controlled experiment was based on a device, where a flat surface represents the surface of a civil engineering structure, e.g., retaining walls, which could be (i) locally deformed by adding an anomaly at the part of the surface, and (ii) broadly deformed by tilting the entire surface. More specifically, the experimental device (Figure 1) consisted of two parts: (i) a flat surface (0.8 m $\times$ 1.2 m) representing the regular flat surface of the facade, and (ii) an anomaly (i.e., bulge), representing a local bulge-type anomaly, which can typically be observed in structures such as retaining walls. The surface of both parts was made by the same material (papier-mâché) and the same color (gray) to mitigate the errors associated with the change in these parameters. To introduce the broader deformation of the surface, the papier-mâché sheet was tilted along its longitudinal axis via ropes that were attached to weights (Figure 1b). The bulge-type anomaly was in a rounded shape with a diameter of 10 cm and a depth of 2.5 cm, and could be attached to the papier-mâché sheet via a bolt (Figure 1c). The depth of the anomaly will be used as the ground truth of deformations for the accuracy measurements in Section 5.

The experiment involves scanning the papier-mâché sheet prior to and after the installment of the surface anomaly. The study investigated two scenarios: (i) the scenario with only local deformation introduced by the bulge; (ii) the scenario combining the global deformation of the surface by applying a tilt to the sheet, and the local anomaly by introducing the bulge. The effect of the scanning geometry was also investigated involving distances varying from 2 m to 30 m, and angles between 0° and 60° (i.e., angle of incidence between 90° and 30°) at a scanning distance of 10 m. Table 1 summarizes the deformation scenarios of the papier-mâché sheet and the scanning setups for the monitoring. The experiment was conducted outdoors with a total of 39 scans. Since all the scans with different angles were conducted from a scanning range of 10 m, there was no need to retake a scan with 0 deg, as it was already taken with the various distances.



(**a**) (**b**) (**c**)

Figure 1. Design of the experimental device (i.e., papier-mâché sheet): (**a**) front view showing the papier-mâché sheet and the anomaly, (**b**) side view showing the introduced tilt, (**c**) rear view for the scenario with no tilt; showing the bolt that was used for attaching the anomaly.

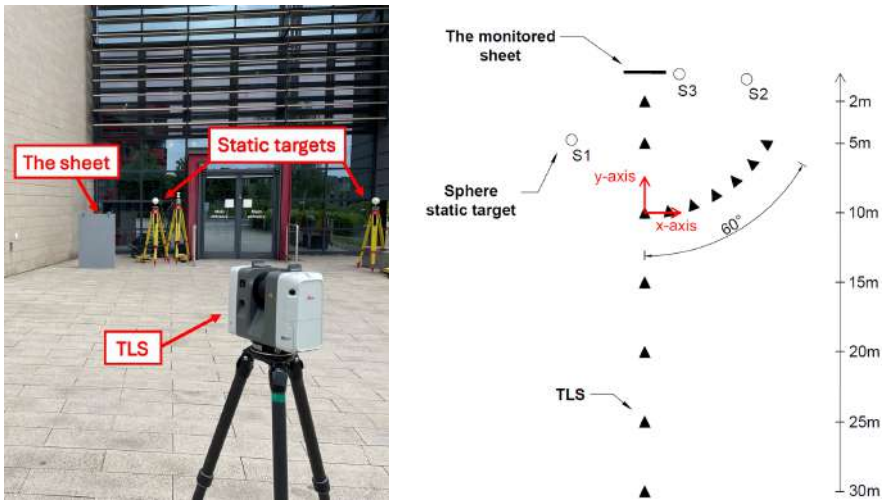
Table 1. Experiment setup for the local geometric deformation experiment.

Scan Setup (for the TLS)		Scenarios of Geometric Deformations
Range (*m*)	**Scanning Angle (°)**	
2	0 * (orthogonal)	initial-undeformed
5	10	Local deformation
10 *	20	Local and global deformation
15	30	
20	40	
25	50	
30	60	

Total number of scans for the TLS = 13 (scanning positions) × 3 (deformation scenario) = 39 scans. * The scan that was taken at a distance of 10 m and the scan with 0° are the same scan.

Three sphere targets were spread and set up at pre-defined control points around the experimental device and were used for the registration of the point-clouds. Figure 2 presents an overview of the conducted experiment, showing the location of the experimental device, the sphere targets that were used for the registration, and the scanning positions from which the TLS was scanning. The laser scanner was set up and used to conduct the measurements at the pre-defined marked scanning positions.

The sheet was scanned using the Leica RTC360 from the thirteen scanning positions (Figure 2) at the initial undeformed state, where the surface was completely flat. Then, the anomaly was attached to the sheet via the attached bolt, considering this the local deformed state of the surface. Finally, the sheet was tilted about its transverse axis using the ropes as shown in Figure 1, considering this the state combining the global broader deformation of the surface and the local bulge-type deformation.



(**a**) (**b**)

Figure 2. Scan setup for the papier-mâché experiment: (**a**) overview of the experiment setup, and (**b**) plan view of the experiment site showing (i) the thirteen scanning positions, (ii) the papier-mâché sheet, (iii) the three sphere targets, and (iv) the final coordinate system (x- and y-axes) that were aligned to the transverse and lateral axes of the papier-mâché sheet.

3. Data Processing and Methodology of Deformation Estimation

The processing consists of three main parts: (i) the definition of the local coordinate system and application of the cloud registration method; (ii) the application of the change detection method; and (iii) the estimation of the magnitude (i.e., depth) of the local of the anomaly by using the C2C, C2M, and M3C2 methods. A summary of the workflow of the research is presented in Figure 3.

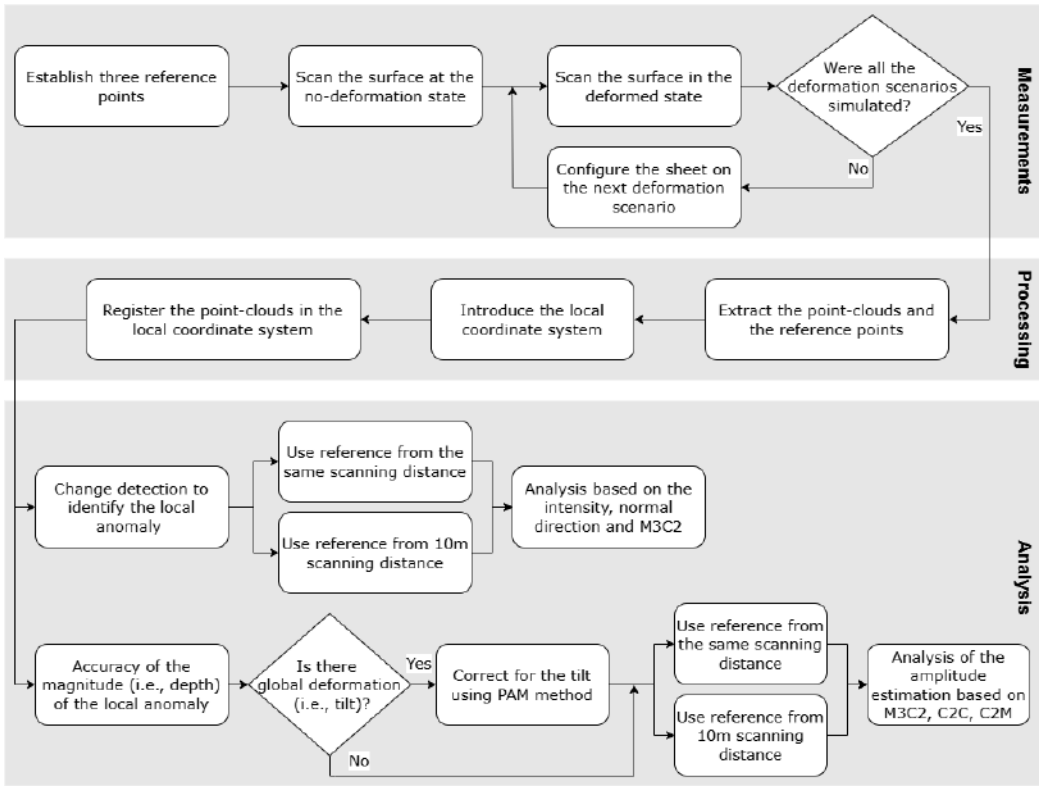


Figure 3. Flowchart of the measurements, processing, and analysis methods.

3.1. Definition of Local Coordinate System and Cloud Registration

The TLS was scanned from thirteen different scanning positions with three deformation scenarios as explained in Table 1. These thirty-nine scans had to be registered in one local coordinate system to allow for the deformation analysis. The local coordinate system was defined using the scan from 10 m. The origin point of the coordinate system for the measurements by the TLS was at the center of the instrument. This coordinate system was rotated in the horizontal plane (i.e., about the *z*-axis) to align the *x*- and the *y*-axes of the local coordinate system to the transverse and lateral axes of the papier-mâché sheet as shown in Figure 2b. The *z*-axis remained the same, pointing upwards along the height of the papier-mâché sheet.

The measurements of the rest of the thirty-eight scans were then transformed to this final local coordinate system using the three static targets (i.e., reference points to align the two coordinate systems) as shown in Figure 2b. The registration was performed based on the Helmert method of coordinate transformation [24] by using the least squares adjustment method to solve for the seven parameters, involving three translations of the origin point along the *x*-, *y*-, and *z*-axes, three rotations about the 3D axes, and a scale factor. This was performed through finding the seven parameters that best fit (i.e., with the minimum sum of the residuals) the three static points in a transformed point-cloud to the reference coordinate system. These three points were used since they represent the same points in both coordinate systems. Figure 4 presents a sample of the three deformation states of the papier-mâché sheet (for the scans that were conducted from 10 m) after the registration of the point-clouds in the local coordinate system.

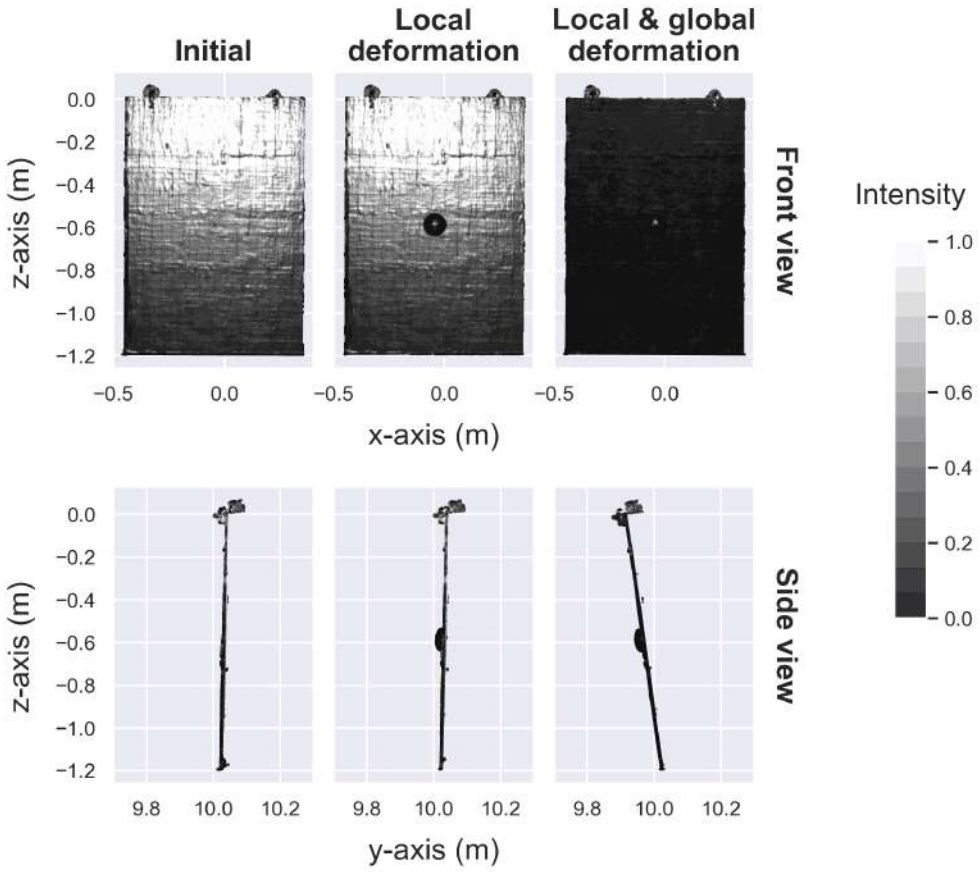


Figure 4. Front and side views showing a sample of the point-clouds at the scanning position of 10 m for the papier-mâché sheet at the three deformation scenarios; (i) the initial undeformed state, (ii) the state where no tilt was introduced but only an anomaly at the center of the sheet, and (iii) the state where both the anomaly and global tilt were introduced to the scanned surface.

3.2. Change Detection of the Facade

The first study was to detect the surface anomaly using the intensity and the change in the direction of the normal vector. The change detection for the surface was executed through four stages for each point P in the reference cloud: (i) defining an imaginary point P^* that has the same y—component as the point P but in the deformed cloud, (ii) finding the neighboring points based on a specific radius r around the point P^*, (iii) defining the new value of the desired parameter (e.g., red color) using the arithmetic mean of the neighboring points, and (iv) calculating the change in colors and normal direction for that selected point P^*, with respect to the point P in the reference cloud through the following equation:

$$\begin{bmatrix} \delta I_i(P) \\ \delta N_i{}^{x}(P) \\ \delta N_i{}^{y}(P) \\ \delta N_i{}^{z}(P) \end{bmatrix} = \begin{bmatrix} I_i(P^*) \\ N_i{}^{x}(P^*) \\ N_i{}^{y}(P^*) \\ N_i{}^{z}(P^*) \end{bmatrix} - \begin{bmatrix} I_0(P) \\ N_0{}^{x}(P) \\ N_0{}^{y}(P) \\ N_0{}^{z}(P) \end{bmatrix} \quad (1)$$

where $[I_0(P)\ N_0{}^{x}(P)\ N_0{}^{y}(P)\ N_0{}^{z}(P)]^T$ represent the intensity and the normal components along the x-, y-, or z-axis for the point P in the reference cloud, $[I_i(P^*)\ N_i{}^{x}(P^*)\ N_i{}^{y}(P^*)\ N_i{}^{z}(P^*)]^T$ represent the arithmetic mean values for these parameters for the neighboring points of the imaginary point P^* at the deformed state i that has the same coordinates as the point P but in the deformed cloud, and $[\delta I_i(P)\ \delta N_i{}^{x}(P)\ \delta N_i{}^{y}(P)\ \delta N_i{}^{z}(P)]^T$ are the changes in the described parameters for the point P at the deformed state i. Therefore, the positive sign of change in the intensity of the reflected laser $\delta I_i(P)$, for example, expresses that the arithmetic mean of the intensities of the neighboring points $I_i(P^*)$ for the point P is larger than the initial value for the point P in the reference cloud $I_0(P)$.

These changes will be presented in a front elevation scatter plot with color representation that shows the amplitude and location of these changes on the facade of the monitored structures. The radius r of which the neighboring points were selected was set to be 0.005 m for all the parameters in the change detection analysis within this research. The radius was kept constant to evaluate its performance for point-clouds with various roughness.

The analysis was performed using two methods: (i) analysis for scans (i.e., the reference and deformed clouds) that were taken from the same scanning position, and (ii) analysis for scans with different scanning positions. In particular, the latter uses the cloud that was taken from a scanning distance of 10 m and scanning angle of 0° as the reference cloud. All the deformed states of the experimental device from all the scanning positions were compared to the reference cloud to investigate the effect of the change in scanning position on the change detection analysis.

3.3. Estimation of the Depth of the Surface Anomaly

The first step in estimating the depth of the anomaly for the case with global deformation (i.e., tilt) was to correct the tilt about the transverse axis by applying the fine registration processing using the Iterative Closest Point (ICP) algorithm. The fine registration was performed with a random sampling limit of 500,000 points that was proposed by the software to provide good results and speed up the processing time. The scale parameter was constrained, while the translations and rotations along/about the three axes were allowed. The condition for which the iterative process was stopped was when the RMS difference between the latest iteration and the one prior was less than 10^{-7}. The local anomaly was then extracted manually for both deformation scenarios (i.e., local deformation, and local and global deformation) by cropping the points with x values between $[-0.15, 0.05]$ m and z values between $[-0.7, -0.5]$ m (Figure 4). The cropping was performed to extract the points within the area of the local anomaly and ensure the exclusion of irrelevant points that could bias the results.

The deformation was estimated using the C2C, C2M, and M3C2 methods. The C2C and C2M methods calculate the distance for each point in the deformed cloud to the nearest point/cloud mesh, respectively, in the reference cloud. The C2C method was improved

by applying a local height function, which selects six neighboring points in the reference cloud to create a local surface of which the distance is estimated. Hence, the first step for the C2C method was selecting a point in the deformed cloud, and then finding the nearest point in the reference cloud. After that, six neighboring points in the reference cloud were used to create the local surface. The C2C method was calculated between the point in the deformed cloud and the local surface in the reference cloud. The C2M method, on the other hand, was executed by first creating a surface mesh of the reference cloud using a "2.5D quadric" equation. Then, the C2M distance between each point in the deformed cloud to the surface mesh of the reference cloud was calculated.

The M3C2 method was executed in two stages. The first stage was defining a local surface for a point in the reference cloud with a specific diameter D that was used to define the normal direction for that local surface. The normal direction was then used as the local axis by which the distance between the two clouds was calculated. The second stage was defining a projection scale d, which was the diameter of the projected cylinder. This was used to define the local surfaces in both the reference and deformed states. The M3C2 distance was estimated as the difference between the two local surfaces. The normal calculation mode was taken in horizontal mode, which allowed the estimation of the direction of the normal vector in the x-y plane.

To accelerate the processing time, two techniques can be applied: selecting core points via sub-sampling the reference cloud, and setting a threshold of the maximum distance L to be calculated. For a better resolution, no sub-sampling of the reference cloud was performed. Table 2 shows the normal scale D, the projection scale d, and the maximum deformation amplitude L that were used in this experiment. The normal scale D and the projection scale d depend on the roughness of the point-clouds, whereas the maximum length of the cylinder L is estimated by the expected deformation. Lague et al. [17] suggested to use a normal scale that is at least twenty times larger than the roughness of the cloud. This is because of the bias that can be involved when the monitored surface is complex (e.g., curved), or the case where the cloud deforms along the transverse axis.

Table 2. Parameters of the M3C2 methods that have been used within this research.

Scanning Position	Normal Scale (m)	Projection Scale (m)	Max. Deformation Amplitude (m)
2 m	0.005	0.005	0.130
5 m	0.020	0.020	0.130
10 m	0.040	0.040	0.130
15 m, 20 m, 25 m, and 30 m	0.050	0.050	0.130
All angles	0.040	0.040	0.130

Both the C2C and M3C2 distances were recorded along the desired axis (i.e., y-axis for lateral displacement), whereas the displacement using the C2M method used the Euclidean distance between the deformed and the reference clouds. The processing of the C2C, C2M, and M3C2 methods was performed via the open-source software, CloudCompare [25] (version v2.12 beta). The depth of the local anomaly was estimated by the maximum distance calculated using the C2C, C2M, and M3C2 methods. The two scenarios, (i) local deformation only, and (ii) local and global deformation (after fine registration), were examined via two methods of analysis: (i) comparing the deformed scans to the initial undeformed scan from the same scanning position, and (ii) comparing the deformed scans with the initial undeformed scan from 10 m.

4. Change Detection of the Facade

In this section, various change detection techniques were applied to the point-clouds of the controlled experiment, including the change in (i) position of the individual points of the point-clouds, (ii) intensity of the reflected laser, and (iii) the direction of the normal

vector for each point in the point-clouds. These changes were applied for the two scenarios of deformation: the case of only local deformation (i.e., bulge), and the case of local and global deformation (i.e., bulge and broader tilt to the sheet).

The first approach is the change in position of the points, which was performed using the M3C2 distance for the two scenarios of deformation (local, and global and local) for the scans that were taken from 10 m (Figure 5). The anomaly was detected at the deformation state of the local deformation as well as the local and global deformation (i.e., anomaly and absolute tilt about the transverse axis). Likewise, the same analysis was conducted for all the scanning positions and for both analysis approaches: (i) when the deformed scans were compared to the initial undeformed scan from the same scanning position, (ii) and for the case when the initial undeformed scan was taken from 10 m. All the cases revealed that the anomaly was detected by the M3C2 method for all the cases and processing approaches (refer to Appendix A).

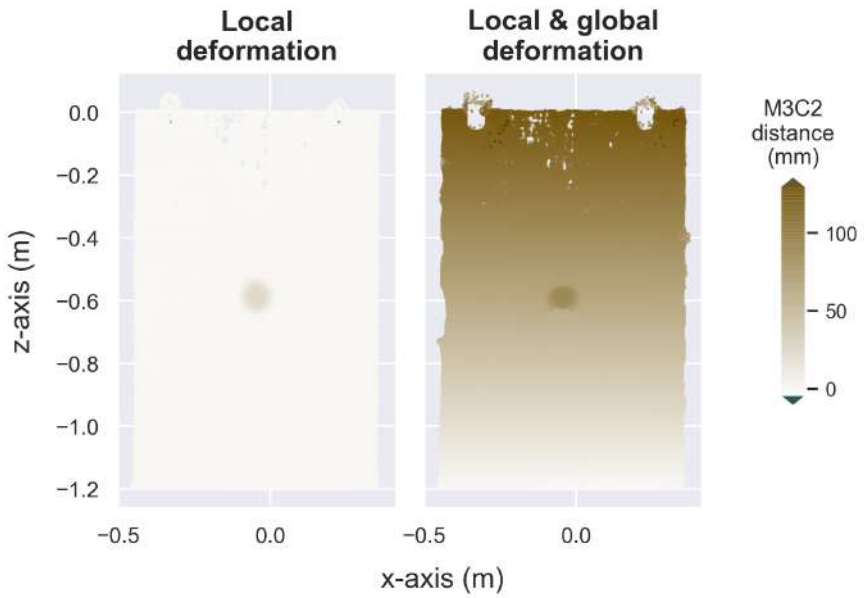


Figure 5. The M3C2 distance for the scanning position of 10 m, compared to the initial undeformed state.

The second approach was the change in the intensity of the reflected laser (Figure 6). The results showed that the change in intensity did not show a clear and constant pattern of results when comparing scans of different distances or angles, making it difficult for the reliable detection of local anomaly (refer to Appendix A for the detailed analysis). It was observed in Appendix A that the change in the intensity was capable of detecting the local anomaly in two conditions: (i) both the reference scans were taken with an angle of incidence of zero, and (ii) there was no broader tilt in any direction of the scanned surface. In these cases, the intensity value was reduced significantly at the area of the anomaly, making the detection of the anomaly clear and reliable. For the rest of the scanned surface, the change in the intensity was very small, expressing the potential noise of the two scans or slight change in the orientation of the surface with respect to the scanner at the given scanning position.

Lastly, the analysis of the normal vector of the points in the point-clouds was conducted to detect the deformation in the two scenarios of the experiment (Figure 7). The results revealed that the change in normal direction along the x- and y-axes was not impacted by the global tilt in the papier-mâché sheet. In contrast, the normal direction along the z-axis was lower for the case of local and global deformation because the tilt in the sheet was along that direction. The change had a negative sign, as the normal vector was pointing more towards the negative side of the z-axis since the tilt was outwards (i.e., towards the TLS). In the same behavior, the anomaly was detected using the change in the normal direction

along the *x*- and *z*-axes as two halves with an increase/decrease in the normal direction with an area in the middle that was not affected (i.e., the white area). However, the areas were divided longitudinally for the change along the *x*-axis, whereas the division was along the transverse axis for the change in normal along the *z*-axis. For the change in the normal direction along the *y*-axis, the results show that it was sensitive to the edges of the papier-mâché sheet, as well as showing the edges of the anomaly. This was consistent for all the point-clouds, and also was not affected by changing the scanning position between the reference and deformed states of the papier-mâché sheet (Appendix A).

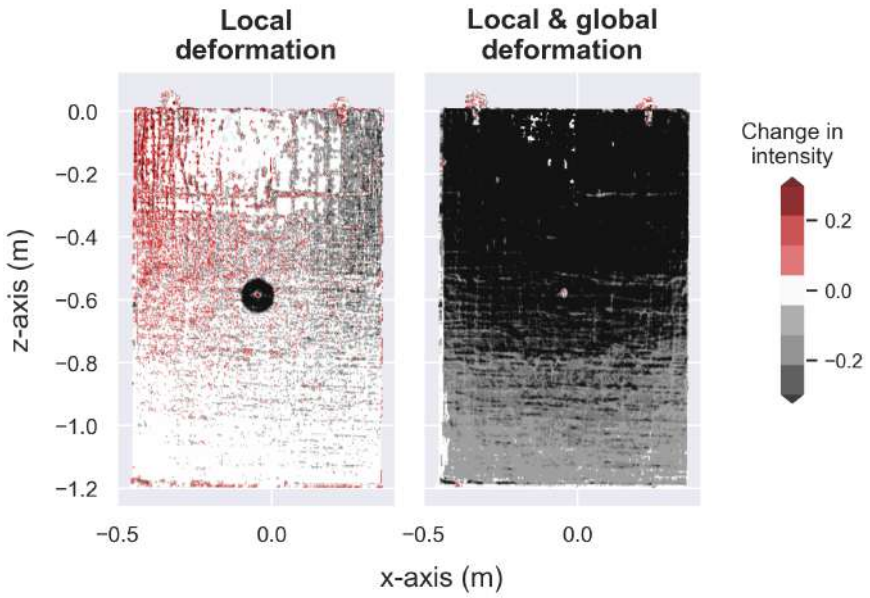


Figure 6. The change in intensity for the scanning position of 10 m, compared to the initial undeformed state.

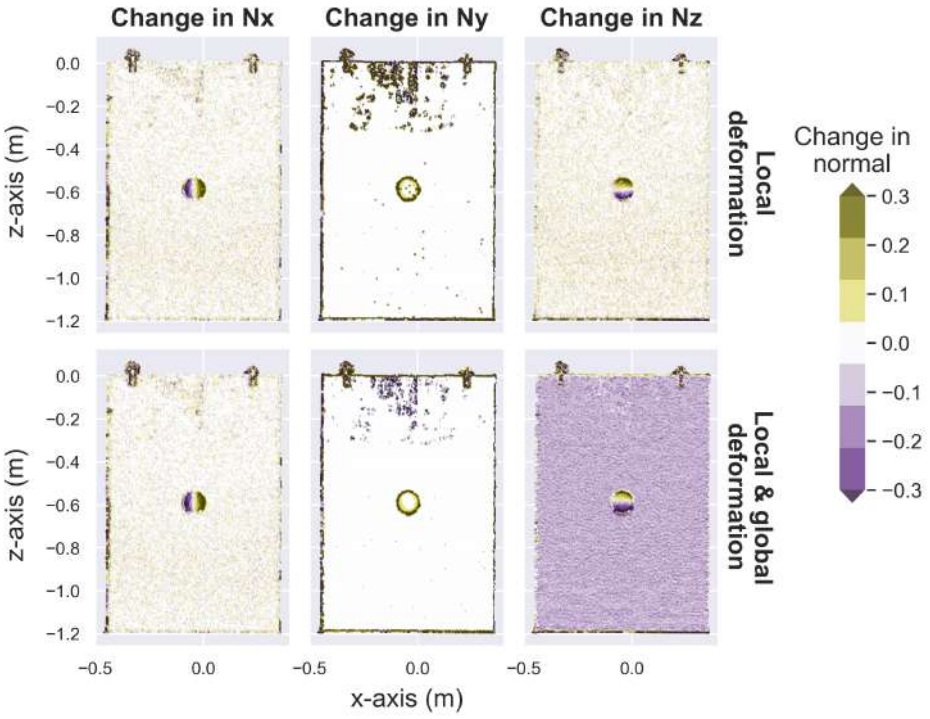


Figure 7. The change in the direction of the normal vector along the *x*-, *y*-, and *z*-axes for the scanning position of 10 m, compared to the initial undeformed state.

5. Accuracy of the Magnitude Estimation of the Local Anomaly

The amplitude of the local anomaly was computed based on the C2C, C2M, and M3C2 methods. The accuracy of the estimation of the magnitude of the local anomaly is plotted in Figure 8 by comparing the deformation estimations with the ground truth measurements using metallic tape. The analysis was based on two cases: (i) where the reference cloud (i.e., the point-cloud at the initial undeformed state) was taken from the same scanning position, and (ii) where the reference cloud was taken as the cloud at the initial undeformed state from 10 m. Both deformation states were presented after correcting the tilt for the case of the local and global deformation scenario.

Figure 8 shows the case where the reference cloud (i.e., the point-cloud at the initial undeformed state) was taken from the same scanning position as well as the case where the reference cloud was taken as the cloud at the initial undeformed state from 10 m. Both deformation states were presented after correcting the tilt in the case of the local and global deformation scenario.

The results show an overall accuracy of within 2–4 mm for all the methods. However, the performance of the M3C2 method was better in most cases (within 1–2 mm) except the case of a scanning distance of 2 m. In this case, the error was much larger for the case where the reference cloud was from the same scanning position (i.e., 2 m) because the M3C2 distance estimates the normal direction of the distance calculated from the local surface in the reference cloud using the neighboring points as explained in Section 3.3. Since the resolution was very high because of the close range scanning in the case of the scanning distance of 2 m, the normal direction was influenced towards the x-axis. In other words, the M3C2 distance was calculated for the diameter of the anomaly, which was 100 mm as mentioned before in Section 3.1, instead of calculating the maximum depth.

The M3C2 distance underestimated the diameter of the anomaly because the anomaly was in the shape of a sphere and not a cube. This issue did not occur when the deformed clouds from a scanning distance of 2 m were compared to the scan from 10 m, as the M3C2 distance estimates the normal direction from the reference cloud and not the deformed cloud. Lague et al. [17] explained how the M3C2 method can under/overestimate the distance between two clouds because of the wrong estimation of the normal direction.

Furthermore, the scanning distance and scanning angle were not significant when the two scans (i.e., prior to and post deformation) were conducted from the same scanning position. The results overall did not show a large variance between the two deformation scenarios (i.e., local deformation, and local and global deformation) and the methods of analysis (i.e., compared to scans from the same or different scanning positions). However, small trends and patterns can be detected. While the C2C method seemed to be more sensitive to the reference cloud, the C2M method was more sensitive to the deformation scenario. This is because the C2C method used a local height function to create a local surface in the reference cloud of which the C2C distance was calculated. The C2M method, however, used a cloud mesh to represent the reference cloud, which mitigates the bias from the density of the point-cloud. Hence, the C2M method was more dependent on the deformed cloud, which was different between the two deformation scenarios. Additionally, both the C2C and C2M methods showed a rise in the error for the scans larger than 20 m as the density of the point-clouds became very small.

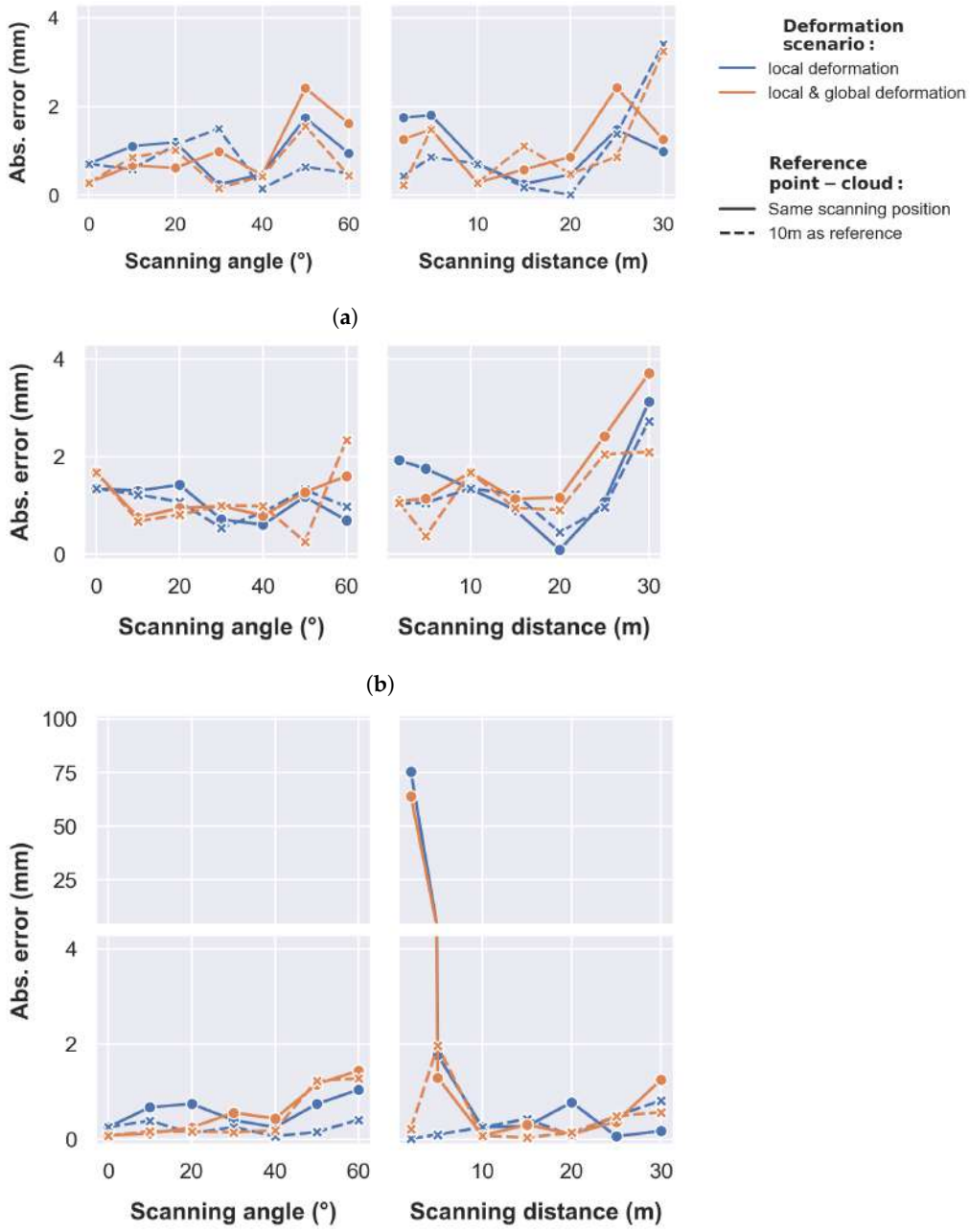


Figure 8. The accuracy of estimating the maximum depth of the anomaly using three cloud-comparison techniques: (**a**) C2C distance, (**b**) C2M distance, and (**c**) M3C2 distance.

6. Application of the Change Detection Techniques

In the above sections, two types of analysis were performed; (i) the identification of the local anomaly, and (ii) the estimation of the accuracy of the C2C, C2M, and M3C2 methods in estimating the magnitude of the local anomaly. Both were based on controlled experiment where different scenarios were simulated, and the scanning was conducted from various scanning positions. For the first analysis, the identification of the local anomaly using the change detection was under the same environmental and weather conditions. The next step was to test the three approaches in detecting anomalies and deformation on an application of the real structural monitoring of a civil engineering structure.

For this purpose, scans were collected for a case study of a structure consisting of (i) a sheet-pile retaining wall, (ii) a capping concrete beam, and (iii) a brick wall facade

(Figure 9). The structure was a new-build student accommodation, where the construction was completed in the summer of 2020. The monitoring of the structure was started just after the completion of the construction and was conducted in five epochs. The scans were collected from roughly the same scanning position and time of the day (i.e., around 10:00 AM) and from a distance of about 18 m.

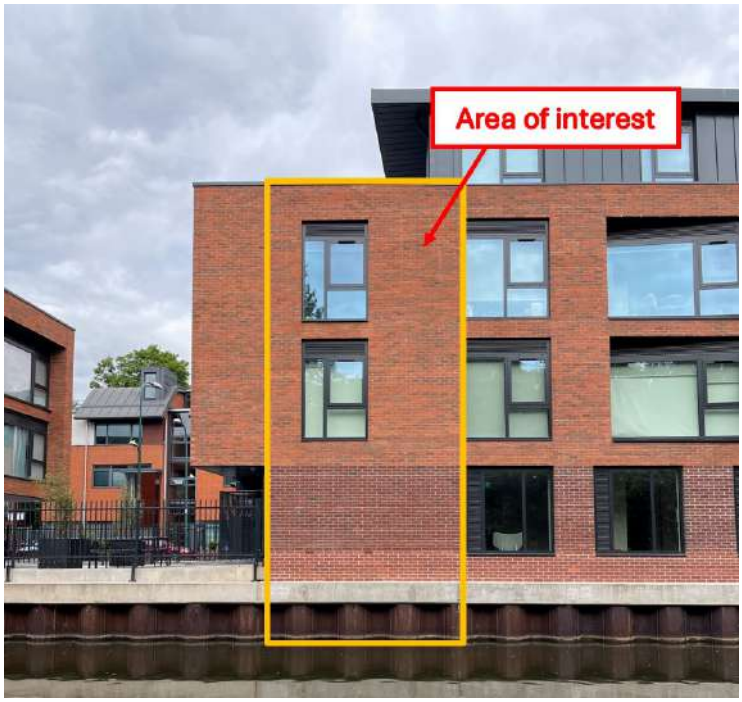


Figure 9. Overview of the monitored case study, showing the area of interest.

The details of the meteorological observations at the time of scanning for each epoch is presented in Table 3 as observed by the Met-Office [26]. The average (three epochs in November) temperature, wind speed, humidity, and MSL pressure were 6 °C, 5.7 Knot, 86.2%, and 1024.3 hPa, respectively, in November, whereas the average (two epochs in June) values in June were 15.4 °C, 5.5 Knot, 60.75%, and 1023 hPa.

Table 3. The environmental condition at the time of scanning for each monitoring epoch.

Epoch	1	2	3	4	5
Date	4 November 2020	9 June 2021	22 November 2021	1 June 2022	3 November 2022
Time	11:00	10:05	10:19	10:24	10:06
Air temperature (°C)	5.8	11.2	5.2	19.5	7.0
Solar radiation (KJ/m^2)	796	426	285	2376	523
Humidity (%)	87.5	69.2	90.3	52.3	80.9
Wind speed (Knot)	6	4	3	7	8
Wind direction (°C)	250	110	250	50	250
MSL pressure (hPa)	1032	1021	1027	1025	1014

The change detection was performed with the same methodology explained in Section 3.2 but with the use of the first scan that was conducted for the first epoch (i.e., 4th of November 2020) as the reference cloud. However, the methodology was first used for the calibration of the change detection results by applying the change detection for scans that were collected on the same day (4 November 2020) from two scanning positions (i.e., orthogonal and oblique with respect to the monitored surface) and at two times of the day (i.e., morning

and afternoon). Only the change in intensity is presented in Figure 10, but the change in the normal vector along the *x*-, *y*-, and *z*-axes is presented in Appendix A in three figures. The results show no deformation detected, as expected, for the independent scans that were taken on the same day.

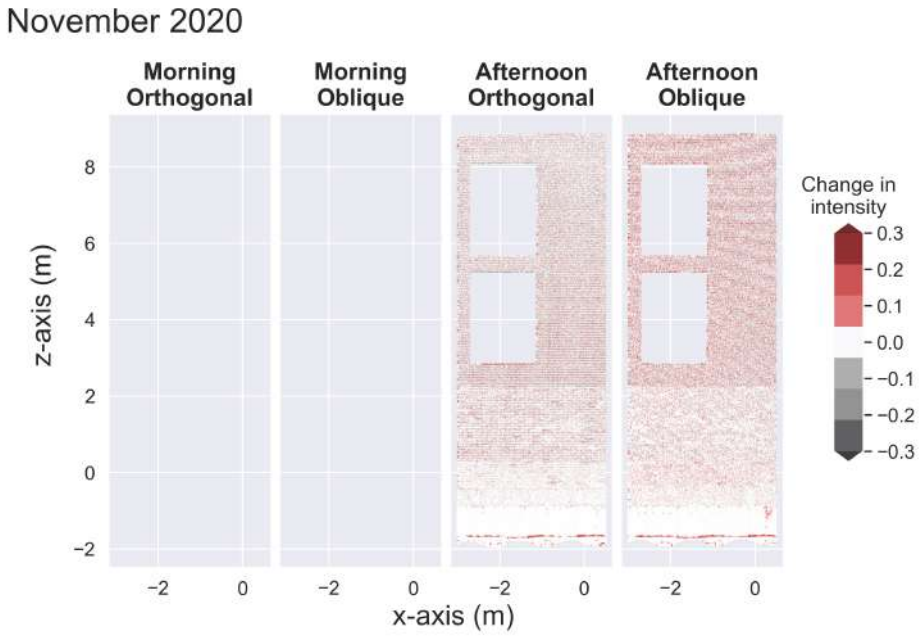


Figure 10. The change in the intensity values for the scans that were taken in November 2020, compared to the reference clouds (i.e., orthogonal and oblique).

The change in intensity of the point-clouds is presented in Figure 11 for the period from November 2020 until November 2022. In general, there was noise in the colors, especially for the points associated with the brick wall. This is because of the difference in intensity between the bricks and the cement mortar. There was no noise observed at the sheet piles due to the very low value of the intensity of the reflected signals. However, the noise was larger in November 2022, which was also observed in a similar laser scanner application and the impact of surface turbidity on the laser scanner intensity (Ranieri et al. [27]).

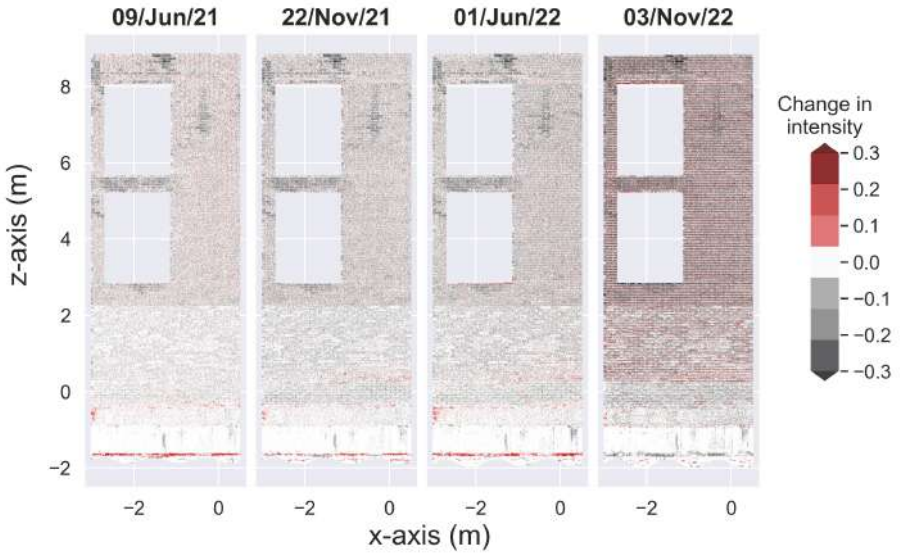


Figure 11. The change in the intensity values for each orthogonal scan that was acquired in the morning of each scanning day, compared to the reference cloud that was taken on 4 November 2020.

In some areas of the point-clouds, it was clearly observed that there was an increase or decrease in the intensity of the reflected laser. More specifically, a horizontal line of the change in the intensity at the lower part of the sheet piles (i.e., along the transverse axis) at the water level of the canal expresses an increase in the intensity in June 2021 and 2022 when the water level of the canal was lower than November 2020 (the reference scan). However, the intensity of the same points was reduced in November 2022 (turned into dark grey) as the water level increased and covered that area. When the water level was at a similar level in November 2021, the line was a mix of red and black zones.

For the brick wall, a loss in the reflected intensity was detected at different areas, mainly near the windows as shown in Figure 11. These changes were detected since June 2021 and remained in the latter epochs, which could be due to potential post-construction treatment (e.g., cleaning, maintenance, and waterproofing) that took place in the period between November 2020 and June 2021 (i.e., the first six to eight months of the structure's age). These changes were detected in all four scans between June 2021 and November 2022 under different scanning conditions (i.e., temperature and humidity), strengthening the validity of the detected changes and the used approach.

Another parameter for the change detection of the wall facade is the change in the direction of the normal vector, which is plotted in Figures 12–14 along the *x*-, *y*-, and *z*-axes, respectively. The change in direction of the normal vector provided consistent performance for the various months, and was very small, indicating no significant change in the surface. However, two bricks were detected to have a noticeable change in the normal direction between the first epoch and the latter epochs. This was because of the material and texture of theses two bricks as shown in Figure 9. Additionally, two lines were detected by the change in normal direction along the *z*-axis near the two bricks with rough textures (with the black boxes in Figure 9). This was identified in November 2021 and remained visible in the latter epochs, suggesting that an additional layer of cement mortar was applied between the bricks in that area.

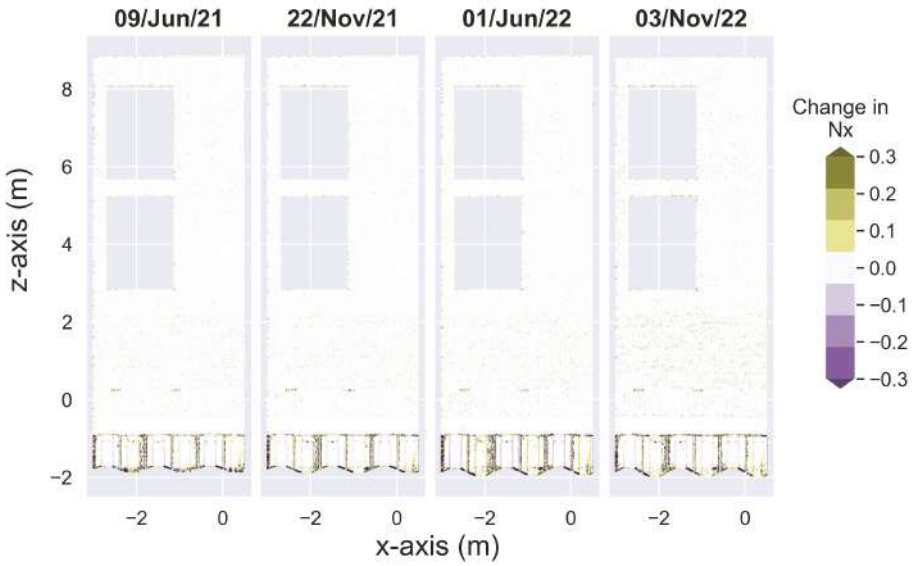


Figure 12. The change in direction of the normal vector along the *x*-axis for each orthogonal scan that was acquired in the morning of each scanning day, compared to the reference cloud that was taken on the 4 November 2020.

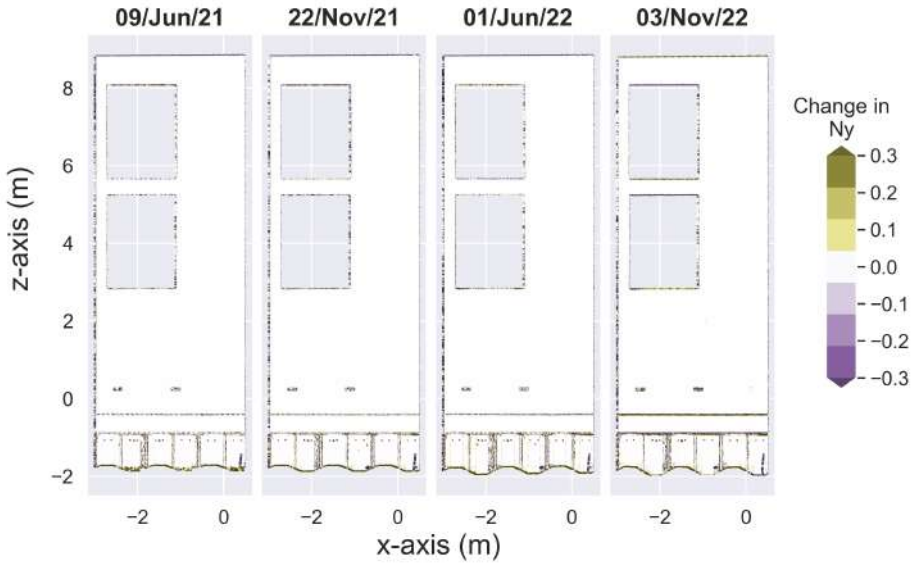


Figure 13. The change in direction of the normal vector along the *y*-axis for each orthogonal scan that was acquired on the morning of each scanning day, compared to the reference cloud that was taken on 4 November 2020.

Since the normal vector was mainly pointing towards the negative *y*-axis, the normal component along the *x*-axis was very small, and therefore only few changes were detected along the *x*-axis. Although the analysis using the change in the normal direction along the three axes was powerful in detecting small changes in the wall facade, it also detected the edges of the scanned surface (clearly detected with the change in the normal vector along the *y*-axis), as well as the anomalies or the abnormal surface material/texture (such as the case of the two bricks). The change in normal direction along the *y*-axis (the one parallel to the normal of the scanned surface) can be the most suitable technique for detecting the outliers and edges of the scanned surface, while the change along the *z*-axis is powerful in detecting the tilt of the scanned surface about its transverse axis.

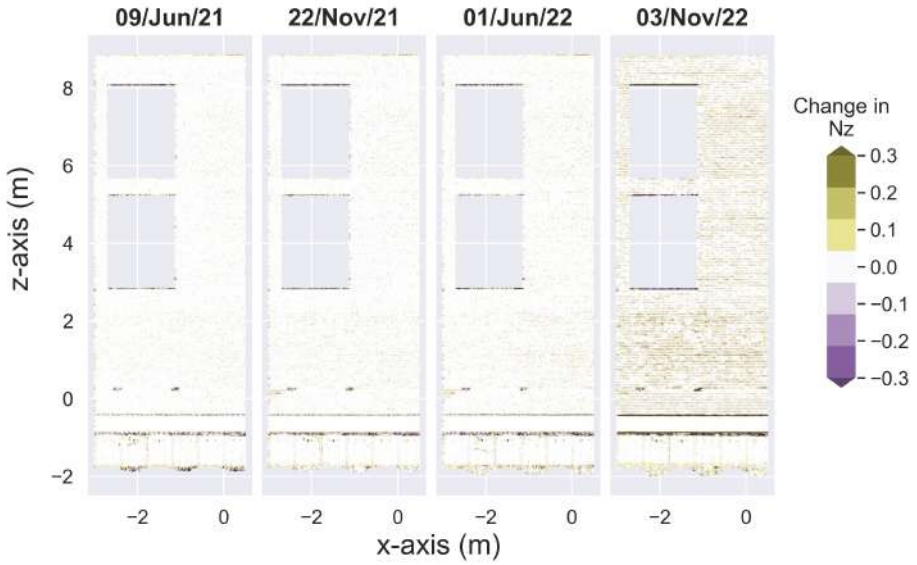


Figure 14. The change in direction of the normal vector along the *z*-axis for each orthogonal scan that was acquired on the morning of each scanning day, compared to the reference cloud that was taken on 4 November 2020.

7. Conclusions and Future Recommendations

The performance of TLS was experimentally assessed for the accurate detection of the local bulge-type anomaly in structures, such as retaining walls. This includes (i) the identification of the local anomaly, and (ii) the accuracy of the estimation of the depth of the local anomaly. A controlled experiment was conducted for various parameters that can affect the performance of the laser scanner including (i) the scanning range (i.e., 2–30 m), (ii) scanning angle (from 0° to 60°), and (iii) techniques to detect the local anomaly (intensity, normal vector, C2C, C2M, and M3C2).

The main outcomes of the experiment showed that the TLS can confidently reveal the surface anomaly when the change detection results are combined (e.g., M3C2 distance, change in intensity, and the change in direction of the normal vector). While the change in intensity was influenced by the scanning position, the M3C2 distance estimation as well as the change in the normal direction were more consistent, regardless of the change in the scanning position. Furthermore, the three cloud-comparison methods (i.e., C2C, C2M, and M3C2) showed good performance in detecting the maximum depth of the anomaly (accuracy within 2–4 mm). Although the M3C2 method was the most accurate (i.e., 1–2 mm), it can over/underestimate the depth of the anomaly because of the biased estimation of the direction on which the distance was calculated. Whereas the C2C method was sensitive to the characteristics of the reference cloud (i.e., initial undeformed cloud), the C2M method seemed to be more influenced by the characteristics of the deformed cloud. The results also showed that the scanning distance and angle did not increase the error budget significantly, especially when comparing two scans (before and after deformation) from the same location.

A case study was conducted for a wall facade over a period between November 2020 and 2022 to investigate the practicality of the change detection techniques with many variables, such as weather. The case study was conducted to assess the impact of the error caused by the registration of the point-clouds, which was mitigated in the conducted experiment (i.e., the experiment with the papier-mâché sheet). The results showed that the change detection techniques were consistent by showing the same changes even at different epochs. The monitoring was conducted in November and June with different weather conditions, showing that the weather did not impact the change detection.

The results of this research can be beneficial for creating deep learning algorithms to detect surface anomalies in wall facades, regardless of the scanning position of the TLS. Further research should also focus on the various (i) sizes and shapes of surface anomalies, (ii) material and color of the scanned surface, and (iii) types of TLS. Finally, an advanced study of how the various shapes and sizes of the surface anomalies in the facade are developed (i.e., predict the cause of the surface anomaly based on the characteristics of the surface anomaly) will be significant in the field of structural health monitoring.

Author Contributions: Conceptualization, A.A., P.P., A.G. and L.N.; methodology, A.A., P.P., A.G. and L.N.; software, A.A.; validation, A.A.; formal analysis, A.A.; investigation, A.A.; resources, A.A.; data curation, A.A.; Writing—original draft, A.A.; Writing—review & editing, P.P.; visualization, A.A.; supervision, P.P., A.G. and L.N.; project administration, A.A.; funding acquisition, A.A. All authors have read and agreed to the published version of the manuscript.

Funding: This research was funded by King Saud University.

Data Availability Statement: The raw data supporting the conclusions of this article will be made available by the authors on request.

Acknowledgments: All our gratitude goes to King Saud University and the Saudi Arabian Cultural Bureau in London for their generous sponsorship for the first author Ali Algadhi to complete his PhD studies.

Conflicts of Interest: The authors declare no conflicts of interest.

Appendix A. Detailed Analysis for the Local Deformation Experiment

This appendix presents the detailed change detection figures for both deformation scenarios (i.e., local deformation, and local and global deformation) at all the scanning positions and by using both analysis methods (i.e., analysis of clouds prior to and after the deformation from the same scanning position, as well as the case where the reference and deformed clouds were taken from different scanning positions).

Firstly, the M3C2 distance was calculated and is presented in Figure A1 for the scans compared to the initial scan from the same scanning position and Figure A2 for the scans compared to the point-cloud at the initial state of the papier-mâché sheet with a scanning distance of 10 m. The results show that the anomaly was detected in all scanning positions and for both analysis methods. However, the scans that were taken from 2 m were not very accurate, as they also showed wrong estimations of anomalies on the surface. The bias was not detected for the case where the initial scan was from 10 m because the direction of the normal vector for the local surface (i.e., the direction of which the displacement was calculated from) using the M3C2 method was estimated based on the points in the point-cloud from 10 m that had less density. In other words, the M3C2 distance was calculated along the transverse axis instead of the lateral axis, and this displacement shows the diameter of the anomaly instead of the depth.

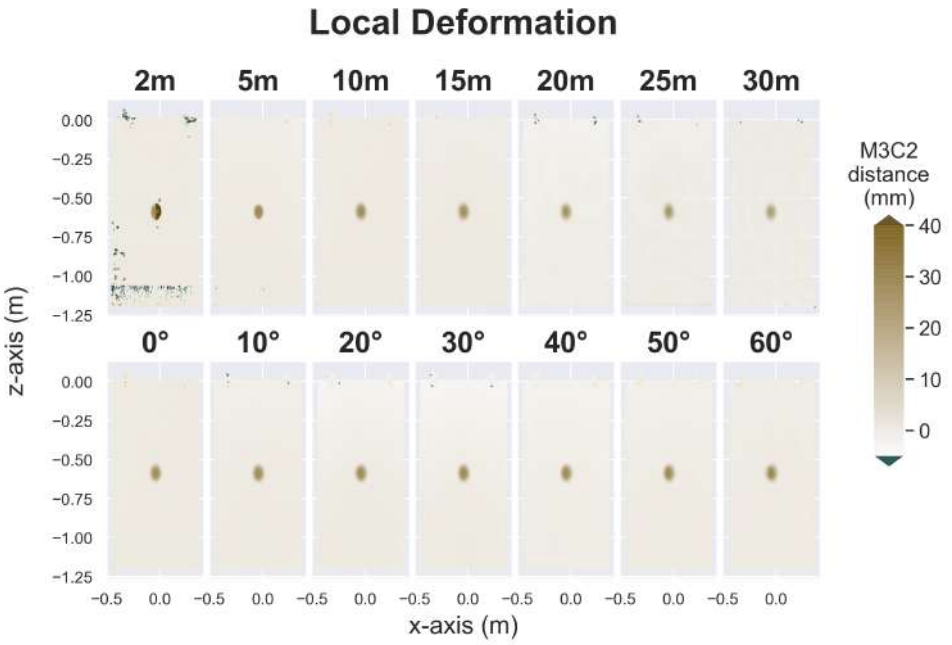
In the case of comparing scans with the initial scan from 10 m especially for the local deformation only in Figure A2a, the results show that the points associated with the two hangers at the top of the papier-mâché sheet were deformed backwards (i.e., away from the TLS) when the angle of incidence increased. This is because the angle of incidence and the beam divergence, which affect the accuracy of the lateral position of the scanned surface. This was observed for the hangers only and not for the papier-mâché sheet, suggesting that this effect is material dependent.

The analysis was also performed for the change in intensity of the reflected signal shown in Figure A3 for the scans that were compared to the initial scan from the same scanning position, and Figure A4 for the scans that were compared to the initial scan from 10 m. The results show the great sensitivity of the change in intensity to the scanning angle. For the scans that were compared to the same scanning position, the change detection was weak for the scans that were not taken perpendicularly (i.e., for the scans from 10°, 20°, 30°, 40°, 50° and 60°). As the scanning distance increases in Figure A1b, the black area increases as well because the decrease in the intensity is caused by the change in vertical angle. For the scan from 2 m, the TLS was very close and at the same level as the top of the papier-mâché sheet (i.e., the magnitude of zero along the z-axis was located at the top of the sheet). In this scan, the bottom of the sheet had a large vertical angle to the scanner, and therefore the change was not noticed clearly. As the TLS moves away from the sheet, a greater area of the sheet has a small vertical angle, and therefore the black area spreads. On the one hand, the anomaly was detected for the case of local deformation only for all scanning distances but with 0° of a horizontal angle, except the case where the TLS was very close (i.e., 2 m) to the papier-mâché sheet.

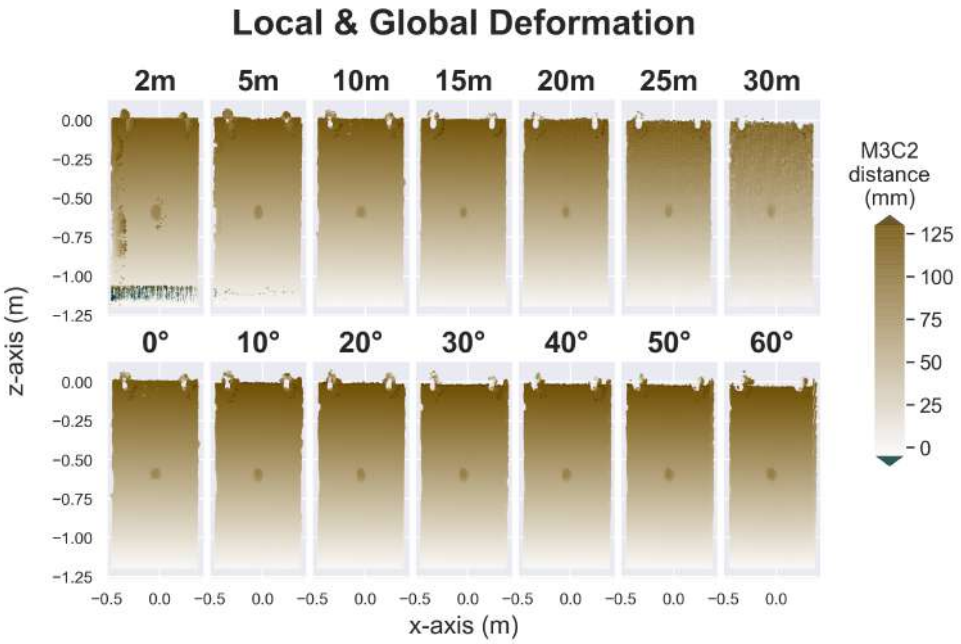
The change in intensity, that is presented in Figure 11, was powerful in detecting the treatment/maintenance on the facade of the monitored structure, compared to the visual detection of changes. For example, the bricks beneath the windows (Figure A5) had various intensities because of the change in material/colors, which led to difficulty in the detection of changes, compared to Figure 11.

Another parameter that was examined is the change in the direction of the normal vector (Figures A6 and A7 for the change along the x-axis, Figures A8 and A9 for the change along the y-axis, and Figures A10 and A11 for the change along the z-axis). The results show both analysis methods, against the initial scan from the same scanning position and the initial scan from 10 m. The results show similar performance for the change along the x- and z-axes. The change is consistent, showing the anomaly clearly. The noise is larger for the scans with a closer distance, indicating that the radius that was used for the change detection was larger than the ideal, and thus a smaller radius would be suitable

to increase the resolution of the change detection. For the change in the normal direction along the *y*-axis, the edges of the anomaly were detected as well as the edges of the sheet. The change along the *y*-axis had the maximum amount of outliers, compared to the change in the normal direction along the *x*- and *z*-axes. In general, the change in direction of the normal vector was a consistent and reliable parameter in detecting the surface anomalies in the papier-mâché sheet, and was not affected by the change in scanning position, which is significant.

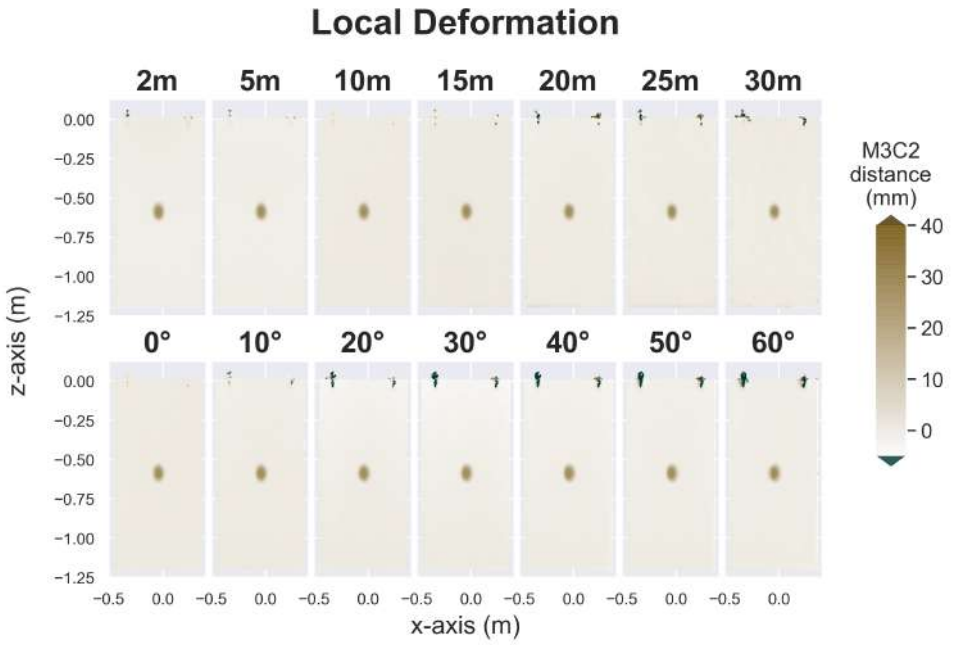


(**a**)

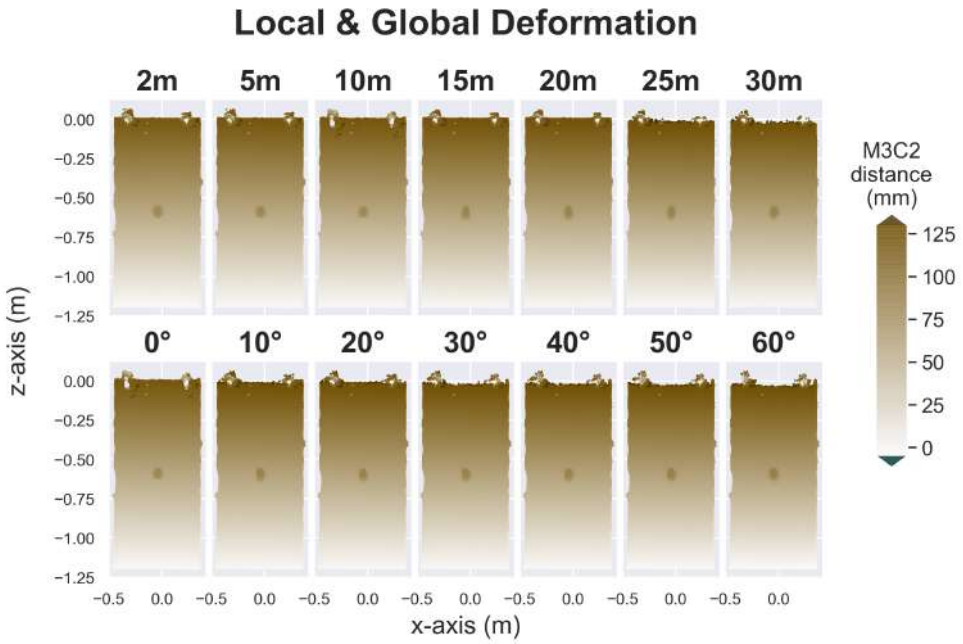


(**b**)

Figure A1. M3C2 distance for the papier-mâché sheet, compared to the initial scan (at the same scanning position) with no anomaly: (**a**) with no tilt, and (**b**) with tilt.

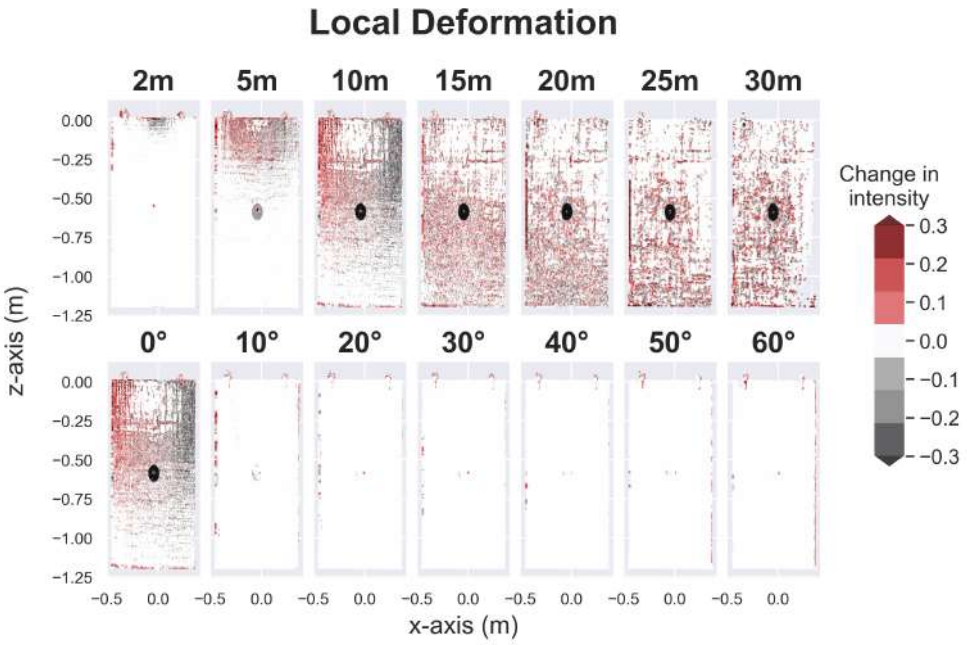


(**a**)

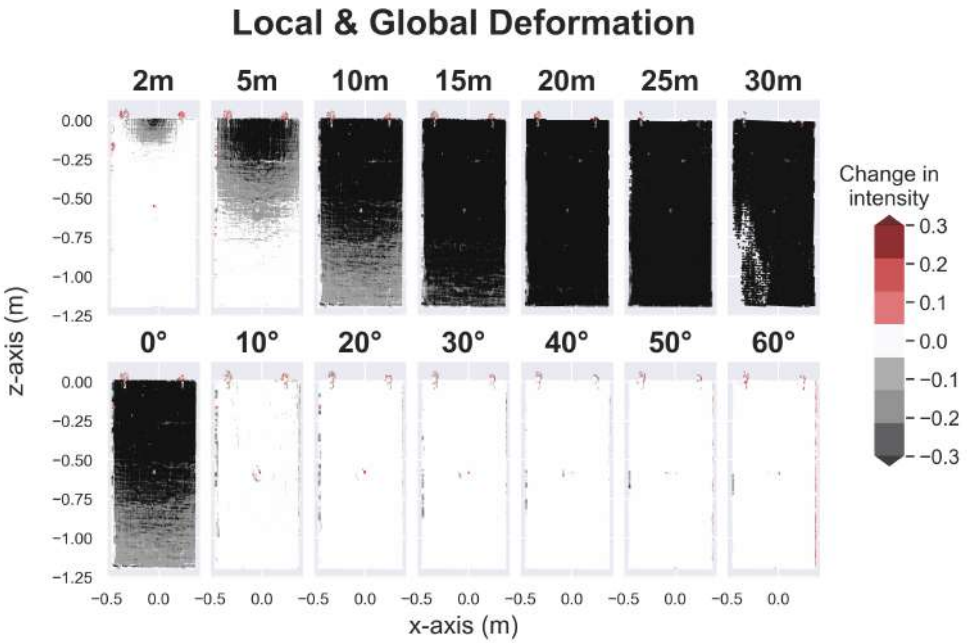


(**b**)

Figure A2. M3C2 distance for the papier-mâché sheet, compared to the initial scan (at 10 m) with no anomaly: (**a**) with no tilt, and (**b**) with tilt.

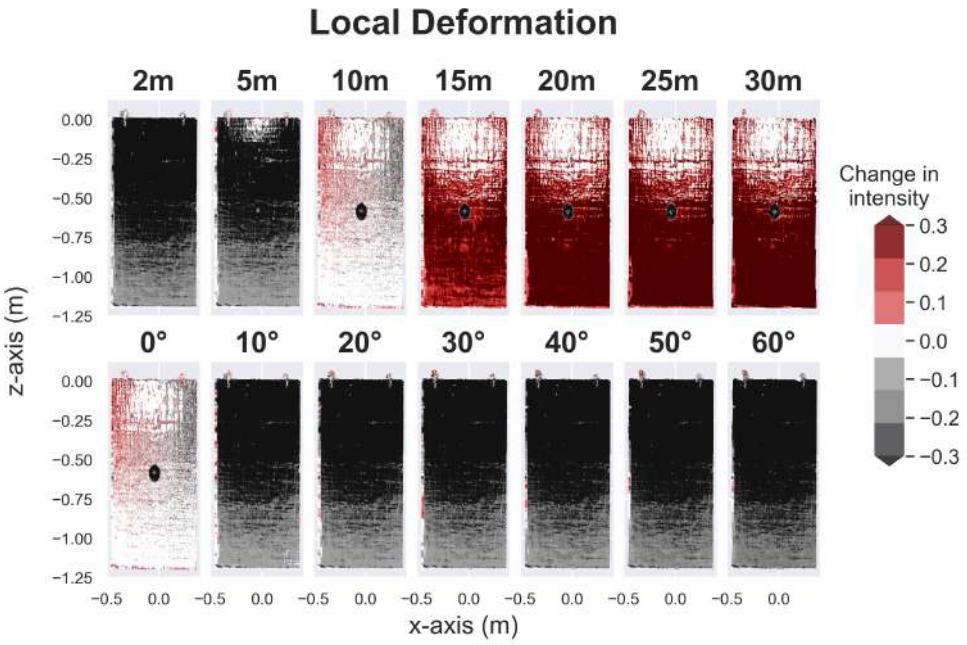


(**a**)

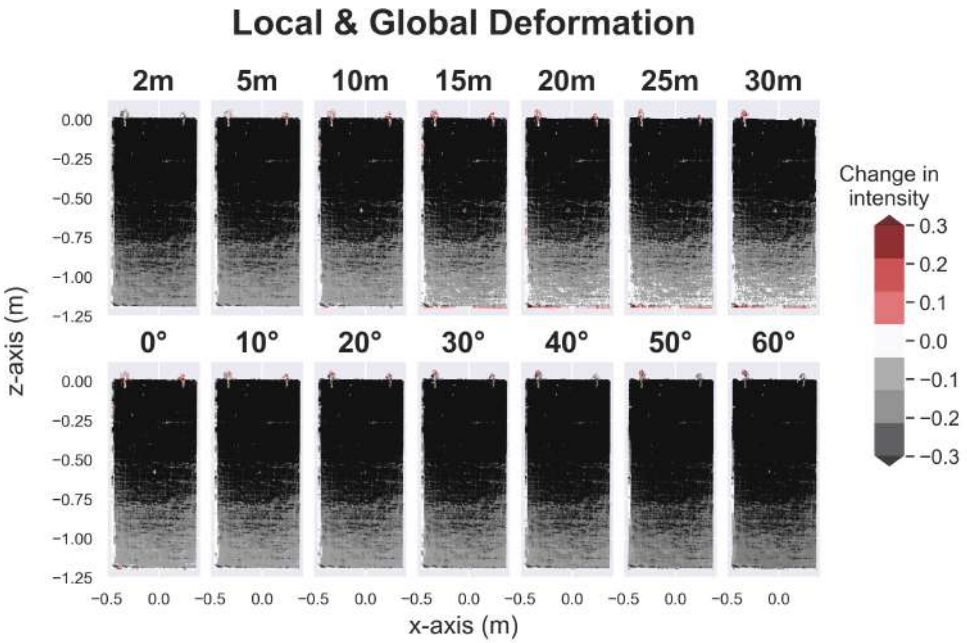


(**b**)

Figure A3. Change in intensity of the papier-mâché sheet, compared to the initial scan (at the same scanning position) with no anomaly: (**a**) with no tilt, and (**b**) with tilt.



(**a**)



(**b**)

Figure A4. Change in intensity of the papier-mâché sheet, compared to the initial scan (at 10 m) with no anomaly: (**a**) with no tilt, and (**b**) with tilt.

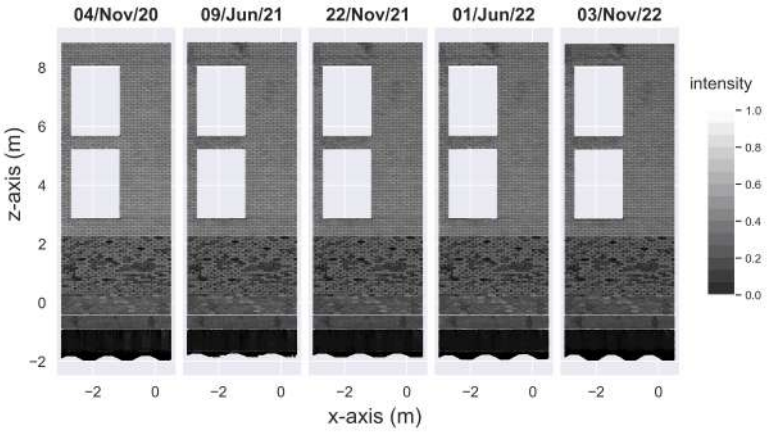
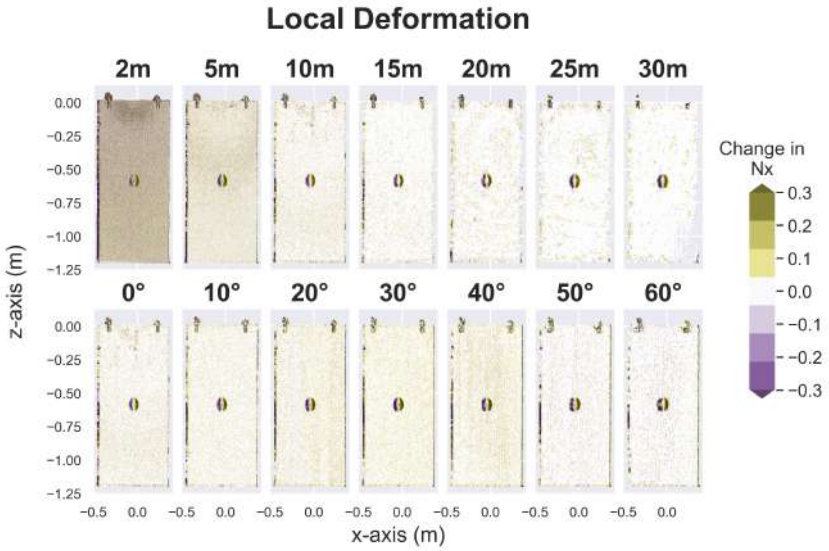
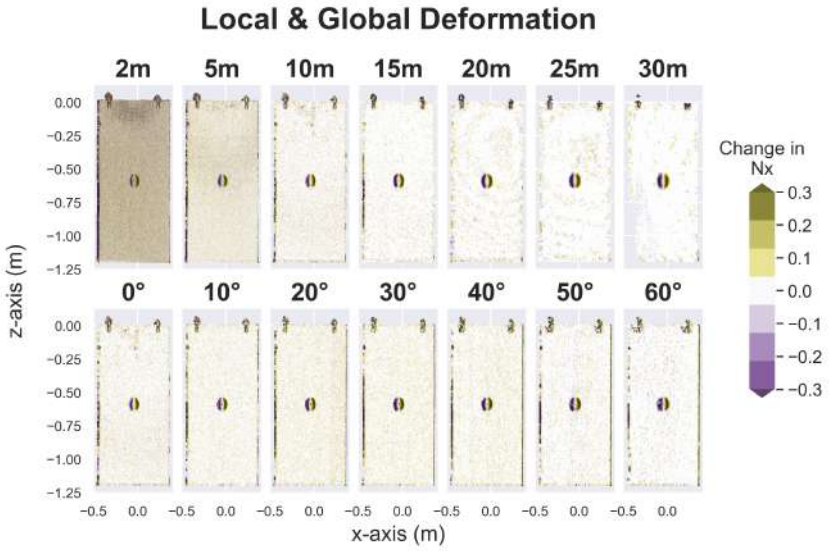


Figure A5. The intensity of the reflected signal on each orthogonal scan that was acquired on the morning of each scanning day.

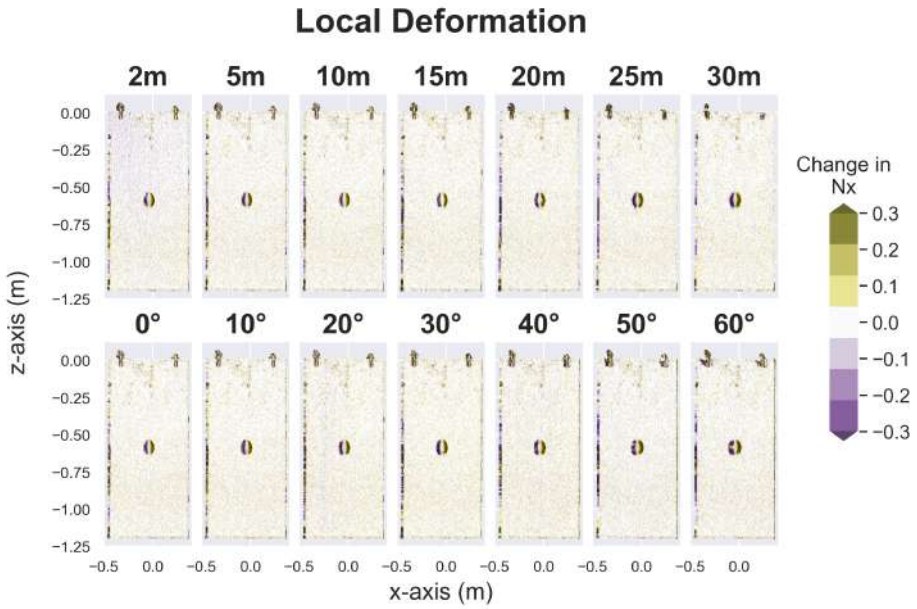


(**a**)

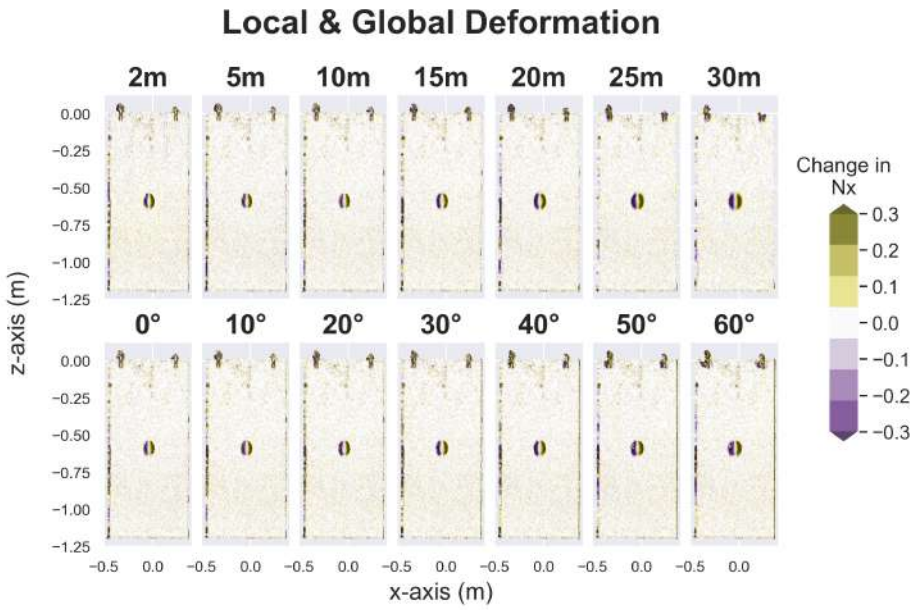


(**b**)

Figure A6. Change in the normal vector along the *x*-axis, compared to the initial scan (at the same scanning position) with no anomaly: (**a**) with no tilt, and (**b**) with tilt.

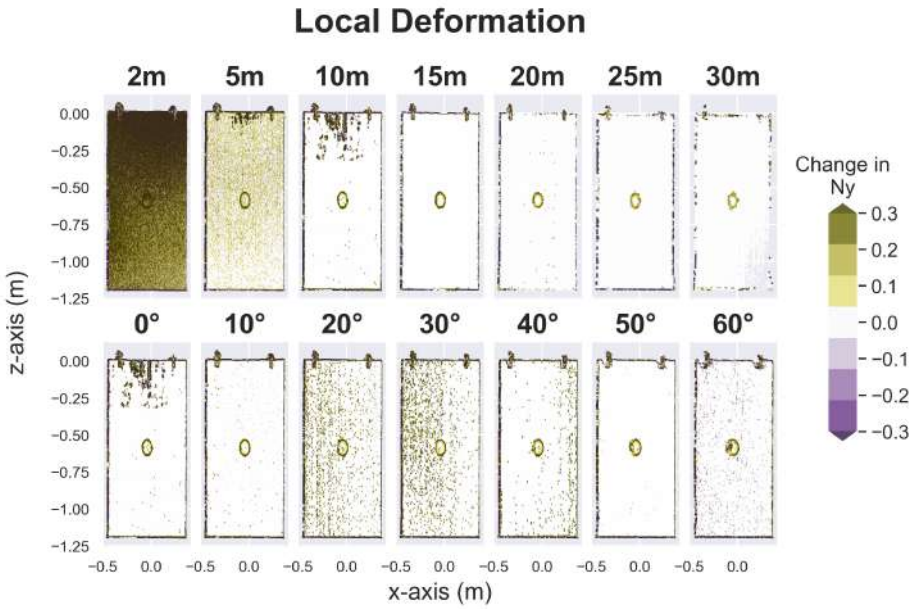


(**a**)

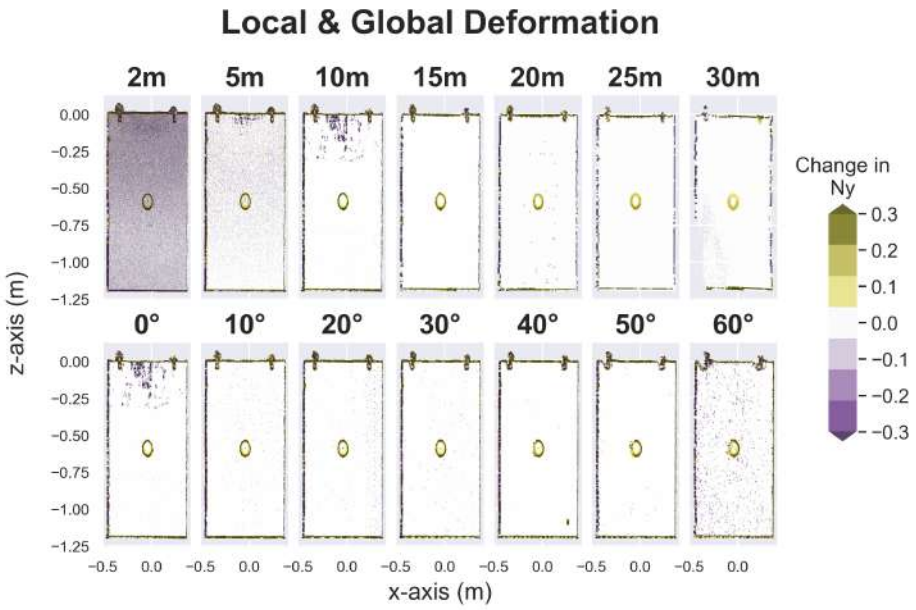


(**b**)

Figure A7. Change in the normal vector along the *x*-axis, compared to the initial scan (at 10 m) with no anomaly: (**a**) with no tilt, and (**b**) with tilt.

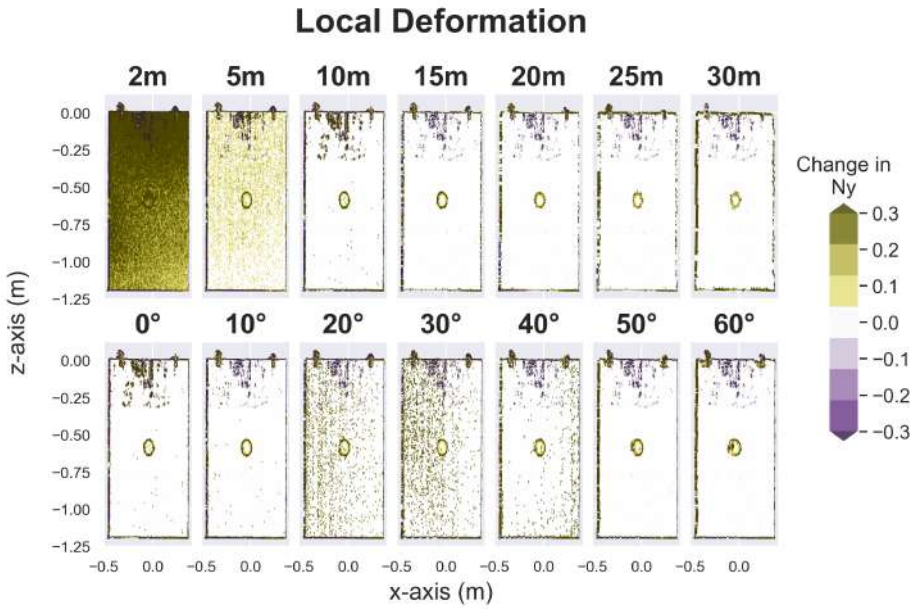


(**a**)

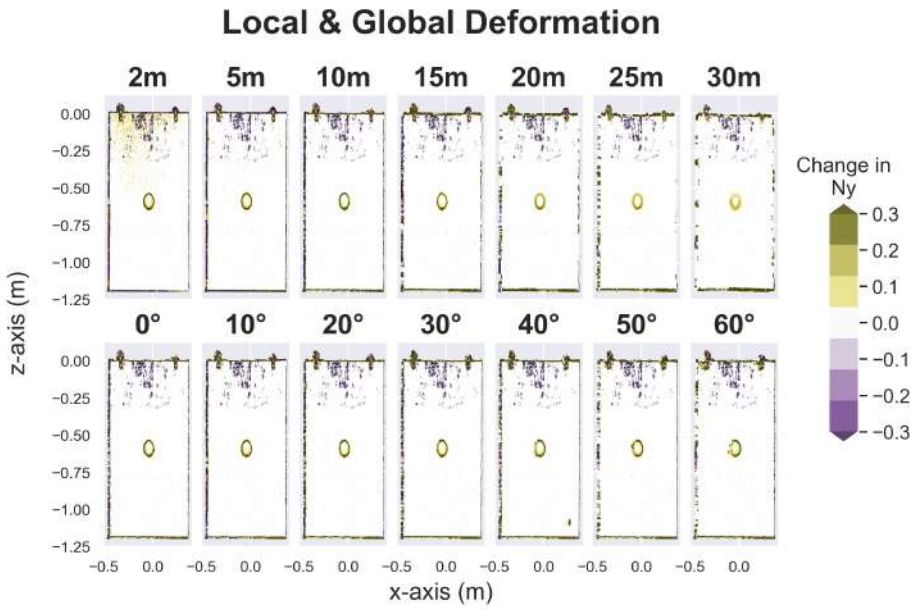


(**b**)

Figure A8. Change in the normal vector along the *y*-axis, compared to the initial scan (at the same scanning position) with no anomaly: (**a**) with no tilt, and (**b**) with tilt.

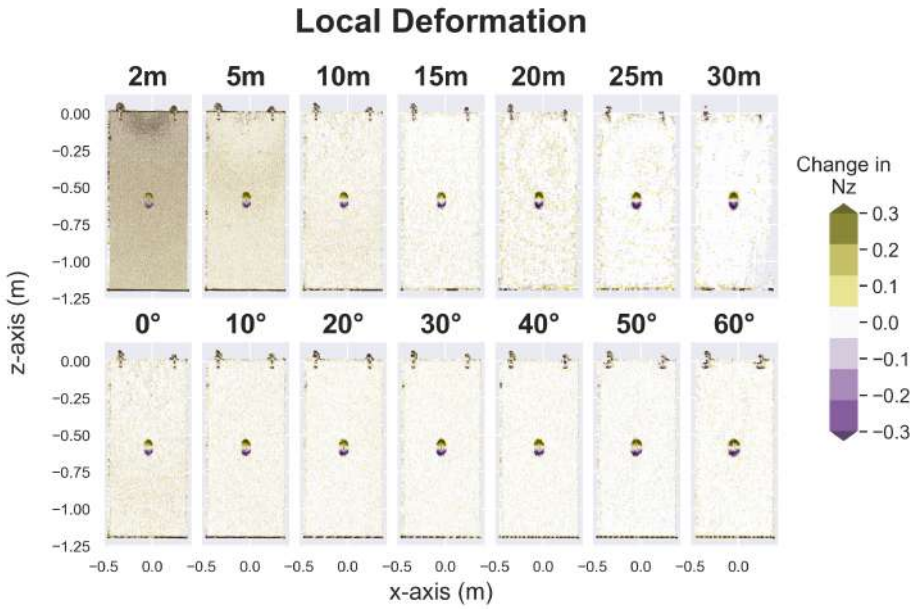


(**a**)

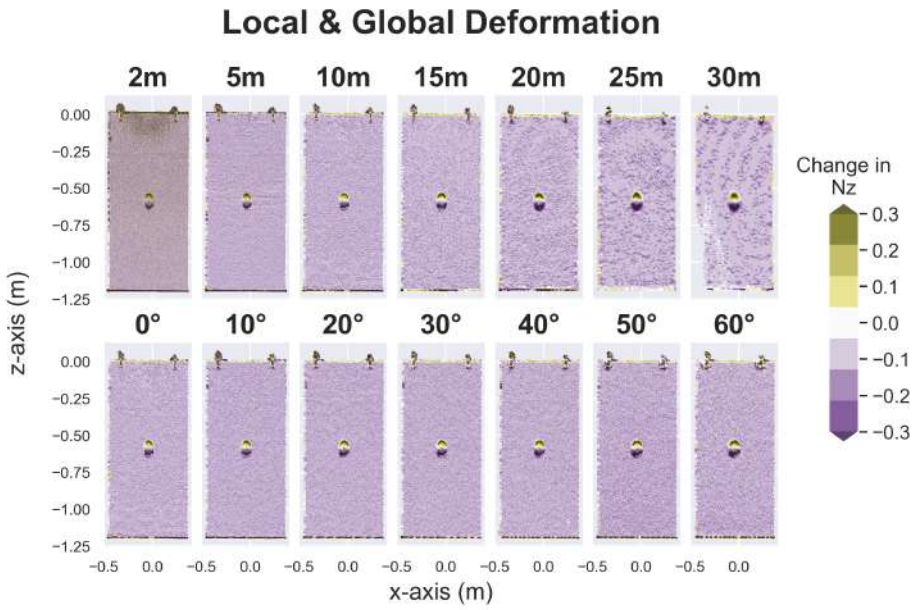


(**b**)

Figure A9. Change in the normal vector along the *y*-axis, compared to the initial scan (at 10 m) with no anomaly: (**a**) with no tilt, and (**b**) with tilt.

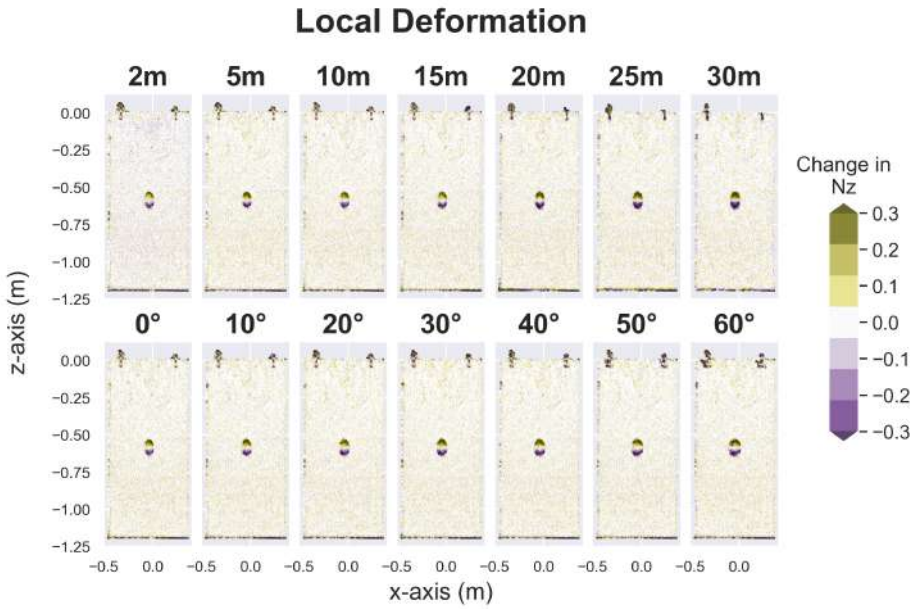


(**a**)

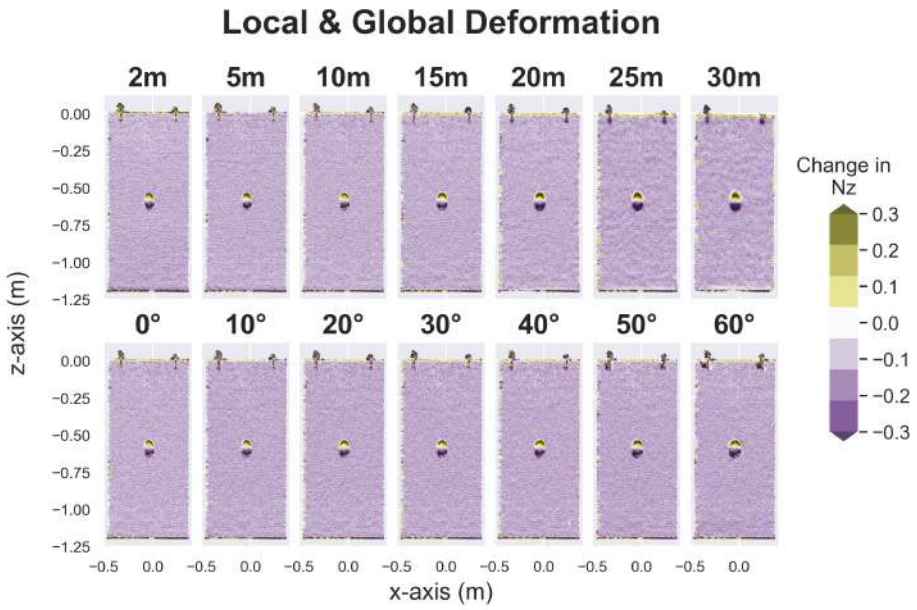


(**b**)

Figure A10. Change in the normal vector along the *z*-axis, compared to the initial scan (at the same scanning position) with no anomaly: (**a**) with no tilt, and (**b**) with tilt.



(**a**)



(**b**)

Figure A11. Change in the normal vector along the *z*-axis, compared to the initial scan (at 10 m) with no anomaly: (**a**) with no tilt, and (**b**) with tilt.

For the monitoring of the case study, the change in the normal vector along the *x*-, *y*-, and *z*-axes for scans that were taken on the same day (4 November 2020) is presented in Figures A12–A14. These changes were detected at the locations of the geometry or the material of the surface because the methodology of the change detection compares each point in the reference scan with a number of selected points around the same location in the deformed scan as explained in Section 3.2.

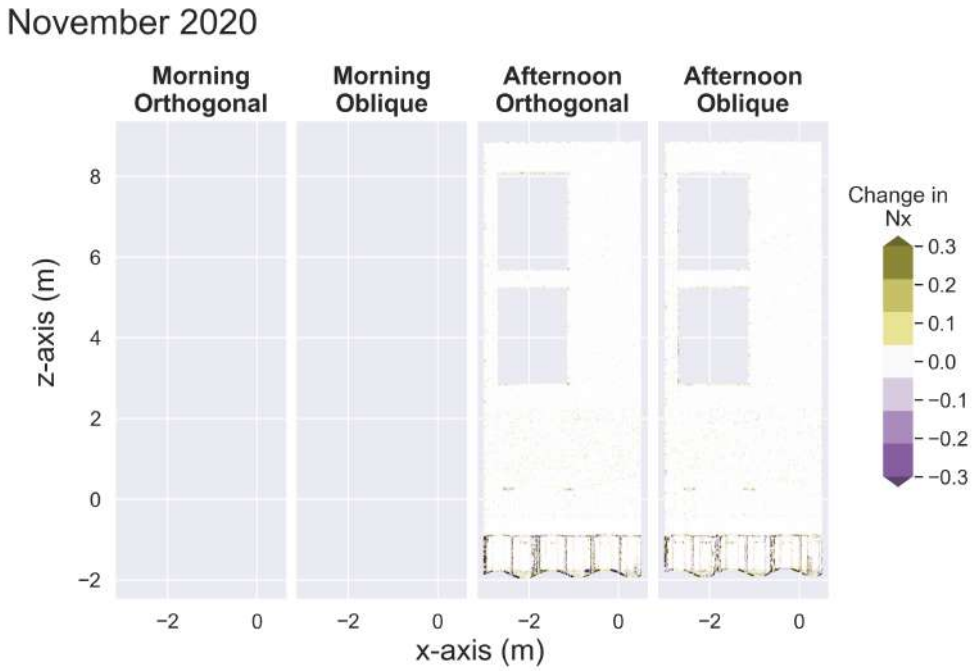


Figure A12. The change in the direction of the normal vector along the *x*-axis for the scans that were taken in November 2020, compared to the reference clouds (i.e., orthogonal and oblique).

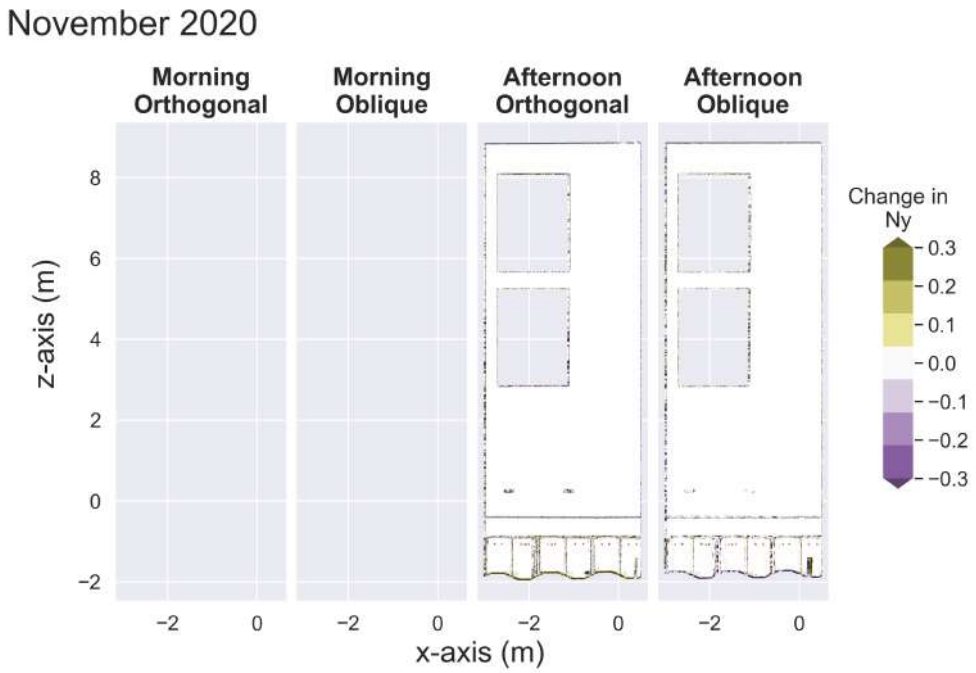


Figure A13. The change in the direction of the normal vector along the *y*-axis for the scans that were taken in November 2020, compared to the reference clouds (i.e., orthogonal and oblique).

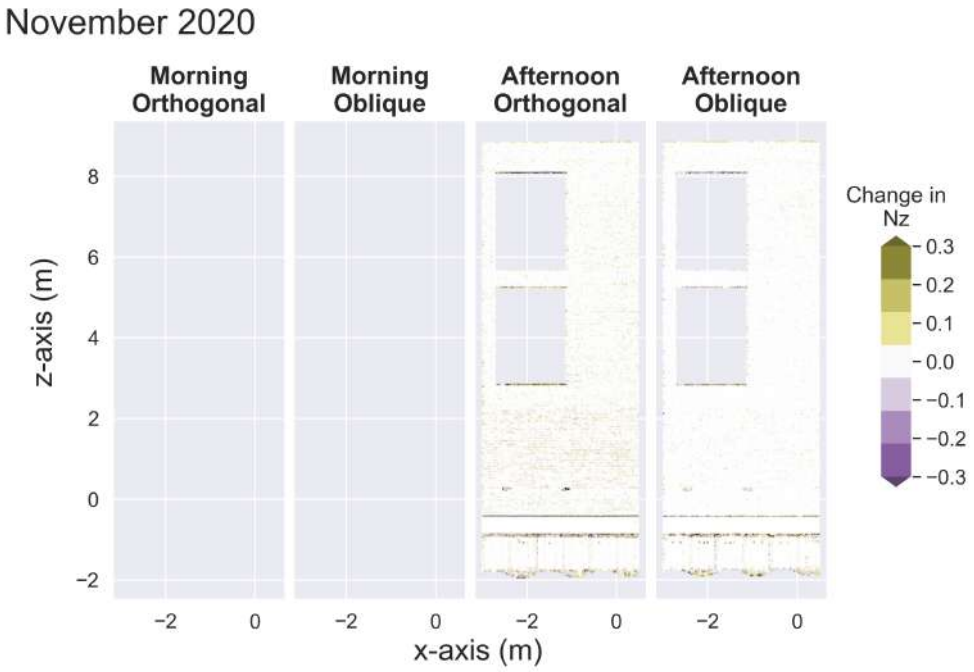


Figure A14. The change in the direction of the normal vector along the *z*-axis for the scans that were taken in November 2020, compared to the reference clouds (i.e., orthogonal and oblique).

References

1. Burland, J.B.; Chapman, T.; Skinner, H.; Brown, M. *ICE Manual of Geotechnical Engineering, Volume 2—Geotechnical Design, Construction and Verification*; ICE Publishing: London, UK, 2012; Volume 2.
2. Long, M. Database for Retaining Wall and Ground Movements due to Deep Excavations. *J. Geotech. Geoenviron. Eng.* **2001**, *127*, 203–224. [CrossRef]
3. Koerner, R.M.; Soong, T.Y. Geosynthetic reinforced segmental retaining walls. *Geotext. Geomembranes* **2001**, *19*, 359–386. [CrossRef]
4. *[CS 450] Inspection of Highway Structures*; Highways England Standards. Highways England: Guildford, UK, 2020.
5. Athanasopoulos-Zekkos, A.; Lynch, J.P.; Zekkos, D.; Grizi, A.; Admassu, K.A.; Benhamida, B.; Spino, R.J.; Mikolajczyk, M. Asset Management for Retaining Walls. 2020. Available online: http://rgdoi.net/10.13140/RG.2.2.11760.89608 (accessed on 10 May 2024). [CrossRef]
6. Lerones, P.M.; Vélez, D.O.; Rojo, F.G.; Gómez-García-Bermejo, J.; Casanova, E.Z. Moisture detection in heritage buildings by 3D laser scanning. *Stud. Conserv.* **2016**, *61*, 46–54. [CrossRef]
7. Suchocki, C.; Katzer, J. Terrestrial laser scanning harnessed for moisture detection in building materials–Problems and limitations. *Autom. Constr.* **2018**, *94*, 127–134. [CrossRef]
8. Chen, S.E.; Liu, W.; Bian, H.; Smith, B. 3D LiDAR Scans for Bridge Damage Evaluations. In *Forensic Engineering*; American Society of Civil Engineers: Reston, VA, USA, 2013; pp. 487–495. [CrossRef]
9. Turkan, Y.; Hong, J.; Laflamme, S.; Puri, N. Adaptive wavelet neural network for terrestrial laser scanner-based crack detection. *Autom. Constr.* **2018**, *94*, 191–202. [CrossRef]
10. Chen, X.; Li, J.; Huang, S.; Cui, H.; Liu, P.; Sun, Q. An Automatic Concrete Crack-Detection Method Fusing Point Clouds and Images Based on Improved Otsu's Algorithm. *Sensors* **2021**, *21*, 1581. [CrossRef] [PubMed]
11. Kim, M.K.; Wang, Q.; Li, H. Non-contact sensing based geometric quality assessment of buildings and civil structures: A review. *Autom. Constr.* **2019**, *100*, 163–179. [CrossRef]
12. Bolkas, D.; Martinez, A. Effect of target color and scanning geometry on terrestrial LiDAR point-cloud noise and plane fitting. *J. Appl. Geod.* **2018**, *12*, 109–127. [CrossRef]
13. Bauer, P.; Woschitz, H. Laboratory Investigations of the Leica RTC360 Laser Scanner—Distance Measuring Performance. *Sensors* **2024**, *24*, 3742. [CrossRef] [PubMed]
14. Kaartinen, E.; Dunphy, K.; Sadhu, A. LiDAR-Based Structural Health Monitoring: Applications in Civil Infrastructure Systems. *Sensors* **2022**, *22*, 4610. [CrossRef] [PubMed]
15. Barnhart, T.; Crosby, B. Comparing Two Methods of Surface Change Detection on an Evolving Thermokarst Using High-Temporal-Frequency Terrestrial Laser Scanning, Selawik River, Alaska. *Remote Sens.* **2013**, *5*, 2813–2837. [CrossRef]
16. Acikgoz, S.; Soga, K.; Woodhams, J. Evaluation of the response of a vaulted masonry structure to differential settlements using point cloud data and limit analyses. *Constr. Build. Mater.* **2017**, *150*, 916–931. [CrossRef]
17. Lague, D.; Brodu, N.; Leroux, J. Accurate 3D comparison of complex topography with terrestrial laser scanner: Application to the Rangitikei canyon (N-Z). *ISPRS J. Photogramm. Remote Sens.* **2013**, *82*, 10–26. [CrossRef]

18. Seo, H.; Zhao, Y.; Chen, C. Displacement Estimation Error in Laser Scanning Monitoring of Retaining Structures Considering Roughness. *Sensors* **2021**, *21*, 7370. [CrossRef] [PubMed]
19. Teng, J.; Shi, Y.; Wang, H.; Wu, J. Review on the research and applications of TLS in ground surface and constructions deformation monitoring. *Sensors* **2022**, *22*, 9179. [CrossRef] [PubMed]
20. Zhao, Y.; Seo, H.; Chen, C. Displacement analysis of point cloud removed ground collapse effect in SMW by CANUPO machine learning algorithm. *J. Civ. Struct. Health Monit.* **2022**, *12*, 447–463. [CrossRef]
21. Kim, J.S.; Lee, G.Y.; Kim, Y. 2D-LiDAR-Sensor-Based Retaining Wall Displacement Measurement System. *Appl. Sci.* **2022**, *12*, 11335. [CrossRef]
22. Makuch, M.; Gawronek, P.; Mitka, B. Laser Scanner-Based Hyperboloid Cooling Tower Geometry Inspection: Thickness and Deformation Mapping. *Sensors* **2024**, *24*, 6045. [CrossRef] [PubMed]
23. Algadhi, A.; Psimoulis, P.; Grizi, A.; Neves, L. Assessment of accuracy and performance of terrestrial laser scanner in monitoring of retaining walls. In Proceedings of the 5th Joint International Symposium on Deformation Monitoring, Valencia, Spain, 20–22 June 2023. [CrossRef]
24. Ruffhead, A.C. Derivation of rigorously-conformal 7-parameter 3D geodetic datum transformations. *Surv. Rev.* **2021**, *53*, 8–15. [CrossRef]
25. CloudCompare. CloudCompare v2.12 beta [Windows 64-bit]. 2021. Available online: http://www.cloudcompare.org/ (accessed on 31 December 2023).
26. Met-Office. Watnall (Nottinghamshire) UK Climate Averages. Available online: https://www.metoffice.gov.uk/research/climate/maps-and-data/uk-climate-averages/gcrje93b8 (accessed on 10 May 2024).
27. Ranieri, C.M.; Foletto, A.V.; Garcia, R.D.; Matos, S.N.; Medina, M.M.; Marcolino, L.S.; Ueyama, J. Water level identification with laser sensors, inertial units, and machine learning. *Eng. Appl. Artif. Intell.* **2024**, *127*, 107235. [CrossRef]

Disclaimer/Publisher's Note: The statements, opinions and data contained in all publications are solely those of the individual author(s) and contributor(s) and not of MDPI and/or the editor(s). MDPI and/or the editor(s) disclaim responsibility for any injury to people or property resulting from any ideas, methods, instructions or products referred to in the content.